Relating the spatial variability of chemical weathering and erosion to geological and topographical zones

Derakhshan-Babaei, Farzaneh ; Nosrati, Kazem ; Tikhomirov, Dmitry ; Christl, Marcus ; Sadough, Hassan ; Egli, Markus

Abstract: The relationship between the spatial variability of soil elements, weathering and erosion rates can be very complex. Topography, abruptly-changing elevation gradients and slopes of varying geological composition exert an important influence on weathering trajectories and erosion. This complex interconnectivity is only rarely addressed in weathering studies. The main objectives of this investigation are, therefore, to relate weathering and erosion to various and geomorphic units in a dry-alpine and threshold landscape having steep slopes (Kan catchment, Tehran Province, Iran). A number of common weathering indices were tested using a genetic algorithm. The best indices are the (K + Na)/Ti ratio, the WIP (weathering index according to Parker), and the PI (product index according to Ruxton). However, the recently suggested 4Si-M+-R2 and M-F-Wmin systems discriminate weathering trends more accurately. Our results show that these soils have a low to moderate weathering stage. Weathering trajectories point to the active formation of kaolinite and oxyhydroxides. River sediments are slightly more weathered and contain the most-weathered topsoils and suggest erosion in the catchment is predominantly due to topsoil removal. Chemical weathering is influenced by the dominant geomorphic units (unconsolidated deposits of the Quaternary and solid bedrock) and landform features (combination of altitude and slope). Aspect does not appear to have a significant impact on weathering. Denudation (erosion) rates were determined using meteoric 10Be since the fluvial sediments did not contain enough quartz for in situ 10Be analyses. This procedure has higher uncertainties due to difficulties in estimating the depositional flux of meteoric 10Be. Due to tectonic uplift, the erosion rates are very high. To maintain a soil layer, soil production rates must be also high. Although annual precipitation is relatively low, slope and soil dynamics seem particularly high, which leads to a fast turnover of the soil material and maintains the weathering intensity at a rather low to intermediate level.

DOI: https://doi.org/10.1016/j.geomorph.2020.107235

Derakhshan-Babaei, Farzaneh; Nosrati, Kazem; Tikhomirov, Dmitry; Christl, Marcus; Sadough, Hassan; Egli, Markus (2020). Relating the spatial variability of chemical weathering and erosion to geological and topographical zones. Geomorphology, 363:107235.
DOI: https://doi.org/10.1016/j.geomorph.2020.107235

Geomorphology 363 (2020) 107235

Contents lists available at ScienceDirect

Geomorphology

journal homepage: www.elsevier.com/locate/geomorph

Relating the spatial variability of chemical weathering and erosion to geological and topographical zones

Farzaneh Derakhshan-Babaei [a], Kazem Nosrati [a], Dmitry Tikhomirov [b], Marcus Christl [c], Hassan Sadough [a], Markus Egli [b,*]

[a] Department of Physical Geography, Faculty of Earth Sciences, Shahid Beheshti University, 1983969411 Tehran, Iran
[b] Department of Geography, University of Zurich, Winterthurerstrasse 190, 8057 Zurich, Switzerland
[c] Laboratory of Ion Beam Physics, ETH-Zurich, 8093 Zurich, Switzerland

ARTICLE INFO

Article history:
Received 1 February 2020
Received in revised form 29 April 2020
Accepted 29 April 2020
Available online 4 May 2020

Keywords:
Weathering indices
Soil spatial variability
^{10}Be
Erosion

ABSTRACT

The relationship between the spatial variability of soil elements, weathering and erosion rates can be very complex. Topography, abruptly-changing elevation gradients and slopes of varying geological composition exert an important influence on weathering trajectories and erosion. This complex interconnectivity is only rarely addressed in weathering studies.

The main objectives of this investigation are, therefore, to relate weathering and erosion to various and geomorphic units in a dry-alpine and threshold landscape having steep slopes (Kan catchment, Tehran Province, Iran). A number of common weathering indices were tested using a genetic algorithm. The best indices are the (K + Na)/Ti ratio, the WIP (weathering index according to Parker), and the PI (product index according to Ruxton). However, the recently suggested 4Si-M^{+}-R^{2} and M-F-W_{min} systems discriminate weathering trends more accurately. Our results show that these soils have a low to moderate weathering stage. Weathering trajectories point to the active formation of kaolinite and oxyhydroxides. River sediments are slightly more weathered and contain the most-weathered topsoils and suggest erosion in the catchment is predominantly due to topsoil removal. Chemical weathering is influenced by the dominant geomorphic units (unconsolidated deposits of the Quaternary and solid bedrock) and landform features (combination of altitude and slope). Aspect does not appear to have a significant impact on weathering. Denudation (~erosion) rates were determined using meteoric ^{10}Be since the fluvial sediments did not contain enough quartz for in situ ^{10}Be analyses. This procedure has higher uncertainties due to difficulties in estimating the depositional flux of meteoric ^{10}Be. Due to tectonic uplift, the erosion rates are very high. To maintain a soil layer, soil production rates must be also high. Although annual precipitation is relatively low, slope and soil dynamics seem particularly high, which leads to a fast turnover of the soil material and maintains the weathering intensity at a rather low to intermediate level.

1. Introduction

Soils play an essential role in controlling the biogeochemical cycle and ecosystem processes (Fitter et al., 2005; Egli et al., 2006; Bogunović et al., 2017) because of the complex interactions with environmental variables and anthropogenic activities (Egli and Poulenard, 2017). Owing to these interactions, the spatial variability of soil properties is often high and, consequently, chemical weathering and erosion are tightly linked to different landscapes and their usage (Goovaerts, 1998). The spatial variability of soil constituents, weathering, erosion etc. is driven by factors (Granger et al., 1996; Riebe et al., 2004; Dixon et al., 2009; Wang et al., 2009; Graly et al., 2011; Heimsath et al., 2012; Larsen et al., 2014; Liu et al., 2015; Wang et al., 2016; Tan et al., 2017; Xiao et al., 2017; Raab et al., 2019) that can be classified into two major groups: i.e. exterior factors, such as agricultural practices and land use type and other inherent factors such as the parent material, climate, soil type and topography.

Chemical weathering is a process in which primary minerals are dissolved or transformed into other minerals. The rate of weathering and mineral transformation and thus soil formation predominantly depends on water, a fundamental length (represented by the granulometry) with respect to water percolation and erosion (Hunt et al., 2015; Egli et al., 2018). At the landscape scale, these processes may strongly vary. Weathering intensity can be measured and classified using various chemical indices (Price and Velbel, 2003). Often, mobile and easily leachable elements are compared to less-mobile components which should thus indicate the degree of weathering. These indices can be used to distinguish the variability of river sediments along longitudinal profiles and to assess soil evolution and fertility. They also may indicate

* Corresponding author.
E-mail address: markus.egli@geo.uzh.ch (M. Egli).

https://doi.org/10.1016/j.geomorph.2020.107235

the impact of climate on parent material weathering, neotectonic metamorphosis, properties of the regolith, and describe the initial dynamics of chemical processes (Neall, 1977; Fedo et al., 1995; Sharma and Rajamani, 2000). Many weathering indices examine the decomposition of unstable minerals. Among them are the Chemical Index of Alteration (CIA; Nesbitt and Young, 1982), the Chemical Index of Weathering (CIW; Harnois, 1988), the Plagioclase Index of Alteration (PIA; Fedo et al., 1995) or the Weathering Index of Parker (WIP; Parker, 1970).

The sum of physical erosion and chemical weathering processes is defined as denudation (Heimsath et al., 1997; Riebe et al., 2001) that varies with time (Mariotti et al., 2019). The rate of physical erosion or denudation (physical erosion is quite frequently approximately total denudation; see Dixon and von Blanckenburg, 2012) is often determined by using isotopic methods such as ^{7}Be, ^{10}Be ($t_{1/2} = 1.4$ My), ^{137}Cs ($t_{1/2} = 30.2$ y), and unsupported ^{210}Pb ($^{210}Pb_{ex}$; $t_{1/2} = 22.3$ y) (Walling and He, 1999; Matisoff and Whiting, 2011). Terrestrial Cosmogenic Nuclides (TCNs) can be used to estimate average denudation rates at the catchment scale in river sediments (Brown et al., 1992; Bierman and Steig, 1996; von Blanckenburg, 2005 and many others). Therefore, TCN contents of river sediments — mostly cosmogenic isotope Beryllium-10 — have been used to estimate denudation rates in diverse climatic and geological zones, different temporal scales and morphological conditions (Norton et al., 2010; Charreau et al., 2011; Portenga and Bierman, 2011; Bekaddour et al., 2014; Granger and Schaller, 2014; Grischott, 2016; Grischott et al., 2017; Marshall et al., 2017; Puchol et al., 2017). In-situ ^{10}Be has been so far the most commonly used technique providing large-scale weathering and erosion data (von Blanckenburg et al., 2012; Wittmann et al., 2016). Much less often, meteoric ^{10}Be has been used to trace earth surface processes such as soil movements (Jungers et al., 2009), the evaluation of landform age (Pavich et al., 1984) or subducted sediments (Morris et al., 2002). Moreover, meteoric ^{10}Be has been used as a tracer for erosion and as a geochronometer (Graly et al., 2011).

Several studies have investigated the relationship between the spatial variability of soil elements, weathering and erosion rates (Hilley et al., 2010; Dixon and von Blanckenburg, 2012; Dixon et al., 2012; von Blanckenburg et al., 2012; Song et al., 2019 and others). The complex interconnectivity of spatial variability of weathering (indices) with topographical features or erosion rates is, however, much less addressed, but this is needed to better explain soil variability and its susceptibility to changes.

The Kan creek is an important catchment of the Tehran Province in central Iran and the main source of water supply for the Lake Chitgar. This region is known to be tectonically active (tectonic uplift; earthquakes) and exhibits abruptly-changing elevation gradients and slopes of varying geological composition. Therefore, this study has the following objectives: 1) evaluation of the relationship between the spatial variability of soil elements and weathering indices at the hillslope scale of the Kan catchment and 2) exploration of the relationship between erosion rates (using ^{10}Be), weathering indices and landscape characteristics using geological and landform (slope and elevation) features.

Based on these objectives we aimed at developing a schematic model that explains the spatial distribution of soil weathering here and the factors controlling catchment-wide erosion characteristics.

2. Study site and sampling strategy

2.1. Study site

The Kan River catchment has an area of about 215 km^2 and is located in the northern part of the Tehran Province, central Iran (Fig. 1). The average altitude, annual precipitation and annual temperature of the catchment are 2377 m, 368 mm and 8.9 °C, respectively (WRI, 2012). The region is characterised by distinct elevation changes, steep slopes (with large parts having a slope of 50–100%; Fig. 2) and a high drainage density. The region is part of the Alborz Zone having the Karaj Formation as its main geological unit, that contains predominantly pyroclastic-volcanic and sedimentary rocks. Alluvial sediments cover limited portions of the catchment, but are particularly distributed in the south of the catchment. The geological characteristics are a critical factor that controls the runoff in the catchment and, therefore, of soil erosion and weathering conditions. The landscape is dominated by mountains. The lowlands are in the southern part of this region. Rangelands and bare land cover about 93% of the catchment area (WRI, 2012). Farmlands and residential areas dominate the remaining 7% of the area.

2.2. Sampling concept

In order to obtain a robust overview of geochemistry and weathering conditions, soil samples were collected from topsoils (0–10 cm, n = 79), subsoils (10–30 cm; n = 41) and from river sediments (n = 23) across the Kan catchment. Samples were taken from the major geologic and geomorphic units (Tables 1 and 2) and at different elevations, slopes and aspects. The sampling of stream sediments at the outlets of each sub-basin was performed in two ways; with bottles and drapes. The drape approach has previously been used in Iran to fingerprint sediments in a region where the collection of suspended sediments was difficult during high flow periods owing to its inaccessibility and remoteness (Nosrati et al., 2018). In addition, a sample of sediment outflow (having a weight of c. 5 kg) from each sub-basin was taken to evaluate the denudation rates.

To account for the dominant landform and geology type of each sub-basin, the geology and terrain properties were evaluated using digital elevation model (DEM) and GIS data. In addition, a landform map was created based on the combination of classified elevation, slope and aspect layers of the region using IDRISI Selva software. In addition, also the TPI (Topographic Position Index; Weiss, 2001) was calculated (Supplementary Table 2). The results of this evaluation are given in Table 1 and Fig. 2.

3. Material and methods

3.1. Chemical analyses

All bulk samples were sieved to <2 mm (fine earth) after drying in an oven at 40 °C for 48 h. The determination of the loss on ignition (LOI; organic matter and adsorbed water) was performed by igniting 2 g of oven-dried fine earth at 550 °C for 16 h.

The analysis of the total elemental content in the fine earth fraction was performed using X-ray fluorescence (XRF). This analysis included major and minor compounds and the Rare Earth Elements (REE) La, Ce, Pr, Nd and Sm. About 5 g soil material was milled to <60 μm and analysed as loose powder in sample cups using an energy dispersive X-ray fluorescence spectrometer (SPECTRO X-LAB 2000, SPECTRO Analytical Instruments, Germany). The carbonate content was determined using a Thermo Fisher Scientific GasBench II connected to a Delta V Plus isotope ratio mass spectrometer (EA-IRMS). Aliquots of samples and standards containing 20–100 μg carbonate C were weighed into EXETAINER® vials, closed and automatically flushed with He for 10 min. 25–50 μl phosphoric acid was then added manually using a syringe (see Egli et al., 2019). Samples were measured at least 60 min after acid addition, which was sufficient to release all carbon from the calcium carbonate, aragonite and dolomite (Breitenbach and Bernasconi, 2011).

To obtain a qualitative overview of samples' mineralogy, DRIFT (Diffuse Reflection Infrared Fourier Transform; Bruker, Tensor 27) measurements of fine earth were performed from 250 to 4000 cm^{-1}. Finely-ground soil material was mixed with KBr (30 mg and 270 mg respectively) and homogenised using a fine ball-mill (Zr) at 10 rpm for 30 s. Prior to measurement, the samples were dried in an oven at

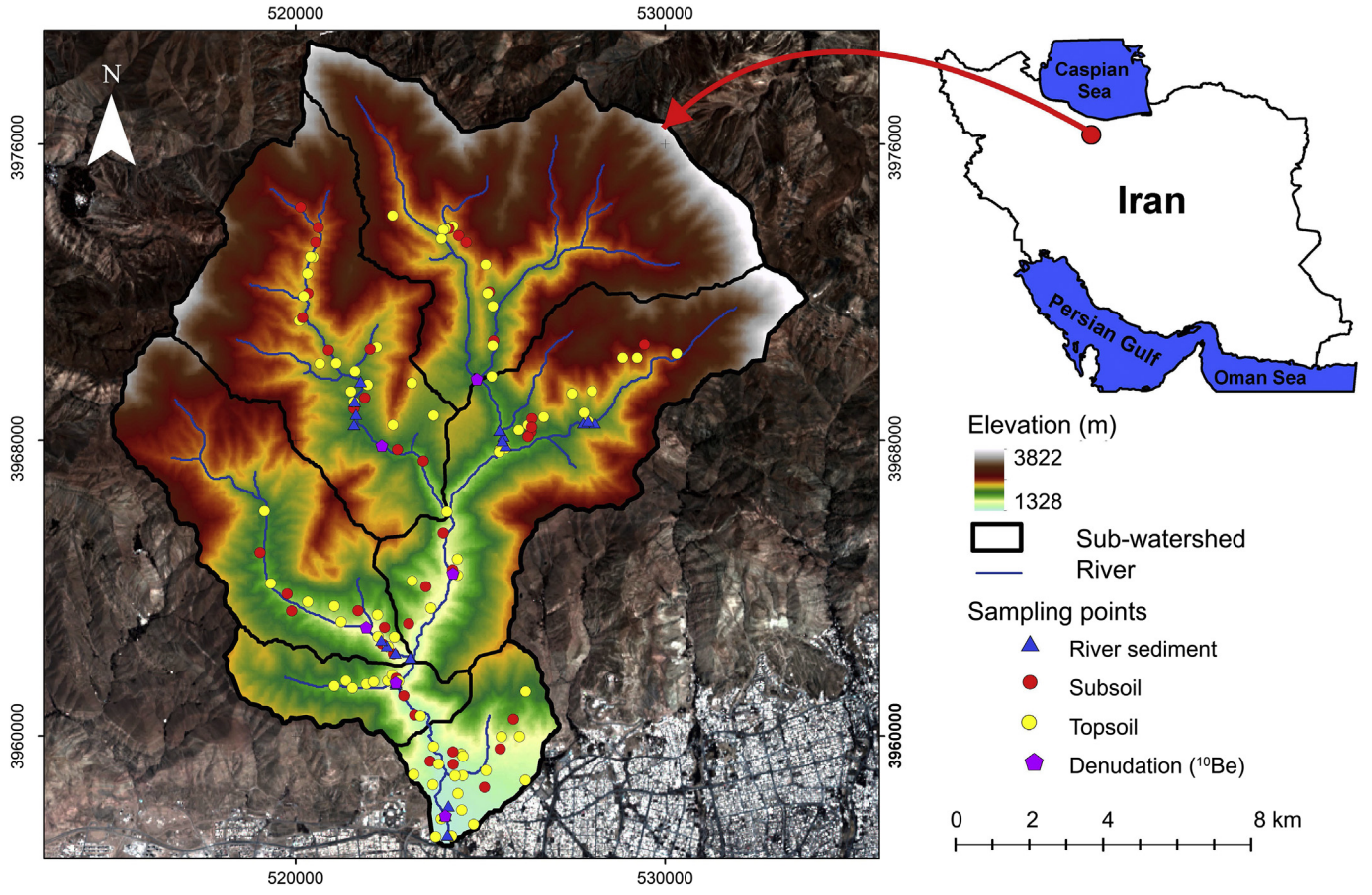

Fig. 1. Geographic location of the study area (Kan catchment), sub-catchments and sampling locations (UTM coordinates).

70 °C for 2 h. The individual spectra were interpreted using OPUS 6 software.

3.2. Chemical weathering indices

3.2.1. Characterisation of chemical weathering using M^+- 4Si-R^{2+} system

To understand the dominant chemical weathering characteristics here, we used the M^+- 4Si-R^{2+} system (Meunier et al., 2013). These authors suggest that any index aiming to measure the weathering intensity cannot be based only on the decreasing amounts of alkali-alkaline earth and divalent metallic components; it must also account for the progressive concentration of trivalent chemical components (R^{3+}). Since the M^+- 4Si-R^{2+} system does not include R^{3+} it must be completed by the inclusion of the weathering intensity scale (WIS):

$$WIS = \frac{R^{3+}}{\left(M^{+} + R^{2+} + R^{3+}\right)} \quad (1)$$

with $R^{3+} = Al^{3+} + Fe^{3+}$; $R^{2+} = Mg^{2+} + Fe^{2+} + Mn^{2+}$ and $M^{+} = Na^{+} + K^{+} + 2Ca^{2+}$ (Meunier et al., 2013; Fang et al., 2019). The M^+, 4Si and R^{2+} amounts are normalised to 100% and subsequently plotted in a ternary diagram (see Fig. 5). These values subsequently were used to calculate the Weathering Intensity Scale (Δ4Si) where:

$$\Delta 4Si = \frac{[(4Si_{soil} - 4Si_{UCC}) \times 100]}{(100 - 4Si_{UCC})} \times 100 \quad (2)$$

$4Si_{UCC}$ denotes the value of the upper continental crust (39.8%; according to Condie, 1993 and Meunier et al., 2013). The 4Si amount corresponds to the number of Si^{4+} cations divided by 4 to refer to the general formula unit of phyllosilicates. A higher Δ4Si denotes a higher degree of chemical weathering (see Fig. 6). The maximum degree is reached when the parent rock is completely transformed into kaolinite (Δ4Si = 100; Fang et al., 2019).

3.2.2. W_{min} index

The weathering index W_{min} was used to determine the degree of weathering of the soils and fluvial sediments combined with the parent rock characteristics from which the soils are developed (Le Blond et al., 2015). The W_{min} index is a good indicator of bulk geochemical alterations that occur during weathering (Ohta and Arai, 2007; Szilas and Garde, 2013; Le Blond et al., 2015). In this study, the W_{min} index was evaluated by using a multivariate analysis of major components in order to estimate the extent of weathering and to characterise the chemical proprieties of the parent rock from which the soils were formed. For this propose, the weight percentage of the eight important oxides (SiO_2, TiO_2, Al_2O_3, Fe_2O_3, MgO, CaO, Na_2O, and K_2O) were considered to calculate the W_{min} index according to Ohta and Arai (2007) and Le Blond et al. (2015). The LOI results were omitted from our database and the remaining variables were normalised to 100 wt% in order to maintain consistency (Ohta and Arai, 2007).

Step 1: The geochemical data were converted into a Euclidean real sample space based on the centred log-ratio transformation (clr-transformation; Eqs. (3) and (4))

$$clr\,(x) = \ln(x_i/g(x))\; i = 1, 2, \ldots, n \quad (3)$$

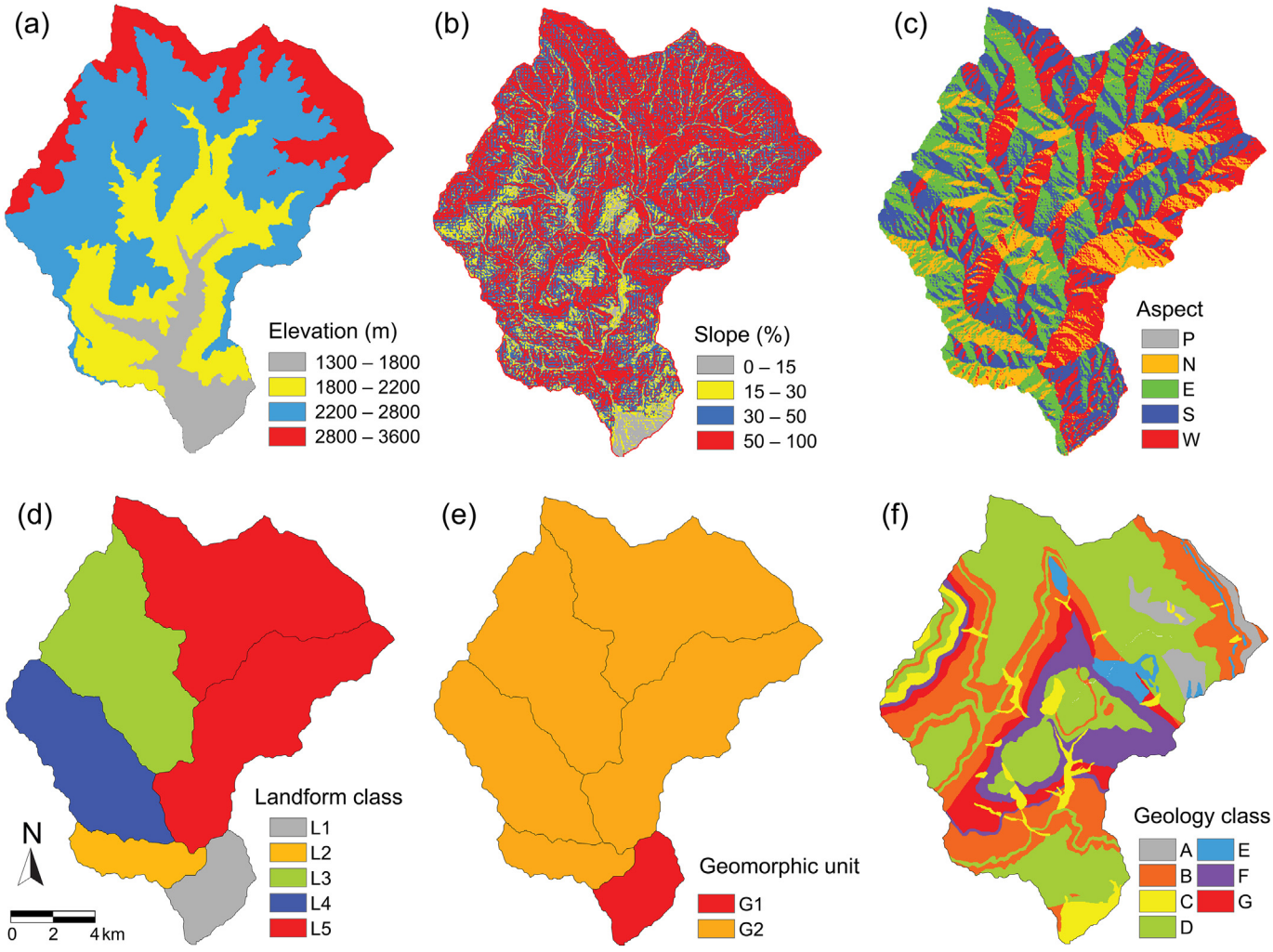

Fig. 2. Classified dominant topographic features of the Kan catchment: (a) elevation, (b) slope, (c) aspect (P = plain, N = north-facing, E = east-facing, S = south-facing, W = west-facing), (d) landform class (cf. Table 1 for details), (e) geomorphic unit (G1 = 1 Quaternary deposits; G2 = solid bedrock) and (f) geology (cf. Table 2 for details).

$$g(x) = \sqrt[8]{SiO_2 \times TiO_2 \times Al_2O_3 \times Fe_2O_3 \times MgO \times CaO \times Na_2O \times K_2O} \quad (4)$$

Step 2: The principal component analysis (PCA) analysis was used to extract two main components (PC1 and PC2) from the results of the clr-transformation.

Table 1
Description of the dominant classes for landform and geology of the study area.

Criteria/class	Dominant feature		
	Elevation (m)	Slope (%)	Aspect
Landform:			
L1	1300–1800	0–15	S
L2	1800–2200	50–100	N
L3	2200–2800	50–100	E
L4	2200–2800	50–100	S
L5	2200–2800	50–100	W

Criteria/class	Dominant feature	
	Characteristics	Dominant rock type (Table 2)
Geomorphology:		
G1	Quaternary deposits	C
G2	Bedrock	D

Step 3: The PCA results were converted to a two-dimensional simplex sample space (see Fig. 7) by the inverse of the isometric log-ratio transformation (ilr-transformation) in order to create a ternary diagram (M, F, W) as follows:

$$V_1 = \exp\left(\frac{-1}{\sqrt{6}}PC1 + \frac{-1}{\sqrt{2}}PC2\right), V_2 = \exp\left(\frac{-1}{\sqrt{6}}PC1 - \frac{-1}{\sqrt{2}}PC2\right), V_3 = \exp\left(\frac{2}{\sqrt{6}}PC1\right) \quad (5)$$

$$C_{100}(V1, V2, V3) = \left(\frac{V_1}{\sum V_1}, \frac{V_2}{\sum V_1}, \frac{V_3}{\sum V_1}\right) = (M, F, W) \quad (6)$$

The ternary diagram (see Figs. 8–9) is used to describe a weathering trend as a "compositional linear trend" based on three vertices, M, F and W_{min} indicating the mafic source (correlated to components such as TiO_2, MgO, Fe_2O_3), felsic source (SiO_2, K_2O, Na_2O) and weathered material, respectively. In other words, the M, F and W_{min} vertices illustrate mafic parent rock, felsic parent rock and the degree of weathering of these rocks or soils. The ternary plots were prepared using the SigmaPlot software.

3.3. Denudation rate determination using cosmogenic ^{10}Be

Determination of in-situ ^{10}Be was not possible due to the fact that the river sediments of the Kan catchment contained a too-low quartz

Table 2
Description of the geological units of the Kan catchment.

Geology class	A	B	C	D	E	F	G
Description	Rhyolitic tuff, lava flow	Green tuff, tuff breccia, shale tuffite with intercalations of tuffaceous siltstone	Old and young terraces, alluvium	Massive green tuff, shale with dacitic and andesitic - basaltic lava flows, green crystal, lithic and ash tuff, tuff breccia, and partly with intercalation of limestone.	Microdiorite-microgabbro as sill and dikes (post lower Eocene)	Sandstone, conglomerate, green tuff	Tuffaceous sandstone, microconglomerate with intercalations of tuffite

content (a sand that provided quartz grains with Ø > 0.1 mm).. As a consequence, we followed the principles of Padilla et al. (2018) and used meteoric ^{10}Be to derive total denudation rates of the main and (sub) catchments. The denudation rate D can be estimated using the following equation:

$$D = \frac{Q}{\rho N_{Surf}} \tag{7}$$

where Q is the meteoric ^{10}Be flux on a specific surface (at m^{-2} yr^{-1}), N_{Surf} is the ^{10}Be content of this surface (at t^{-1}) and ρ the density (t m^{-3}).

The most critical parameter in Eq. (7) is the estimation of ^{10}Be flux Q. In this study, we used three different approaches to estimate Q and consequently we present three versions of denudation rates (Table 3). The first two versions rely on model data from Field et al. (2006), Heikkilä (2007) and Willenbring and von Blanckenburg (2010). The third version was based on an empirical approach presented by Graly et al. (2011) according to which Q is at any mid or low latitude L and any precipitation P:

$$^{10}Be_{flux} = P\left(\frac{1.44}{1+e^{\left(\frac{(30.7-L)}{4.36}\right)}} + 0.36\right) \tag{8}$$

Meteoric ^{10}Be was extracted from the river sediments using a modified method from Horiuchi et al. (1999) and Egli et al. (2010). A sample of 2 g of the river sediment (<2 mm fraction) was milled to fine powder and ignited at 550 °C for 3 h to remove organic matter. Thereafter, 1 mg of ^{9}Be carrier in the form of $Be(NO_3)_2$ and 8 ml of 16% HCl were added to the sample and leached overnight in a shaker. After centrifugation, the liquid containing BeCl was collected. The solid part of the sample was leached overnight a second time in 5 ml of 16% HCl to ensure full extraction of ^{10}Be. The leachates were combined and the pH of the solution was increased to 2 using a NaOH solution. 1 ml of a 10% EDTA solution was added to the sample to prevent formation of metal complexes such as Fe and Mn and the pH of the sample increased to 8 to precipitate the gel containing $Be(OH)_2$ and $Al(OH)_3$.

Table 3
Denudation (~erosion) rates (based on meteoric ^{10}Be, Eq. (7)) in the subcatchments of the Kan catchment.

Subcatchment	Denudation using Input Q1	Denudation using Input Q2	Denudation using Input Q3
	mm yr^{-1}	mm yr^{-1}	mm yr^{-1}
Sulagan	0.353	0.151	0.156
Keshar	0.620	0.265	0.275
Heriyas	0.174	0.074	0.077
Rendan	0.388	0.166	0.172
Taloon	0.058	0.025	0.026
Davood	0.063	0.027	0.028

Q1: ^{10}Be depositional flux according to Heikkilä (2007) and Field et al. (2006): 1.17 × 10^{10} atm m^{-2} yr^{-1}.
Q2: ^{10}Be depositional flux according to Willenbring and von Blanckenburg (2010): 0.5 × 10^{10} atm m^{-2} yr^{-1}.
Q3: ^{10}Be depositional flux according to Graly et al. (2011): 0.519 × 10^{10} atm m^{-2} yr^{-1}.

At pH 14, $Be(OH)_2$ and $Al(OH)_3$ re-dissolved in the solution and was separated from $Fe(OH)_3$ gel by centrifugation. Thereafter, 1 ml of EDTA was added to the sample at pH 2, and the gel containing $Be(OH)_2$ and $Al(OH)_3$ was precipitated at pH 8 using NH_4OH and centrifuged. The hydroxides were dissolved in 20 ml of 0.4 M oxalic acid and Be was separated from Al using the cation exchange resin Bio-Rad AG50-X8. After reduction of the sample volume, $Be(OH)_2$ was precipitated using NH_4OH. The resulting $Be(OH)_2$ gel was dried and calcinated for 2 h at 850 °C in the oven to obtain BeO. Finally, the BeO was mixed with Nb powder and pressed into a sample holder for accelerator mass spectrometry (AMS).

The ^{10}Be/^{9}Be ratios were measured at the ETH Zurich AMS system Tandy (Christl et al., 2013) and normalised to the ETH Zurich in-house AMS standard S2007N (^{10}Be/Be = 28.1 × 10^{-12} nominal), which has been calibrated relative to ICN 01-5-1 (^{10}Be/^{9}Be = 2.709 × 10^{-11} nominal) (Nishiizumi et al., 2007) — both associated with a ^{10}Be half-life of 1.387 ± 0.012 My (Chmeleff et al., 2010; Korschinek et al., 2010). The measured and standard normalised ^{10}Be/^{9}Be ratios were blank corrected using full processed blanks (Table 7).

3.4. Spatial variability and landscape analyses

The spatial variability of soil elements, oxides and weathering indices (Table 4) was compared to topographic features derived from the digital elevation model (DEM) of the study area using the SAGA software. In addition, four zones were extracted based on topographical features using the hierarchical clustering (dendrogram) method of the SPSS software. With a hierarchical clustering, data grouping is performed based on the similarity of topographic features of the samples. Each node in the hierarchical tree represents a group having similar topographic features. The considered number of soil elements, oxides and weathering indices were 39, 8 and 26, respectively. The genetic algorithm (GA) in MATLAB was used to specify the best weathering indices (Table 4) in relation to the spatial variability of soil elements and oxides in each zone. One-way ANOVA analysis was used to evaluate the differences between the best indices (via GA) in the topographic zones. The relationship between determined weathering indices and elements was then evaluated using a correlation test (Pearson, SPSS software).

3.5. Statistics

Chemical data and weathering indices were compared with each other as a function of the geology and landscape type. Datasets were first checked for normal distribution by a Shapiro-Wilk test (SigmaPlot 11.0, Systat Software Inc.; Jann, 2005). To perform multiple comparison tests for non-parametric data, a one-way ANOVA (Kruskal-Wallis test) was applied using SigmaPlot 11.0 (Systat Software Inc.; Jann, 2005).

4. Results

4.1. Main geochemistry, mineralogy and weathering trends of the sites

All topsoil, subsoil and river sediment samples are characterised by an intermediate (from mafic to intermediate-felsic) chemical

Table 4
Description of the weathering indices or indicators.

Weathering index	Equation	Reference
WIP	$[2Na_2O/0.35 + MgO/0.9 + 2K_2O/0.25 + CaO/0.7] \times 100$	Parker (1970)
CPA	$[Al_2O_3/(Al_2O_3 + Na_2O)] \times 100$	Buggle et al. (2011); Cullers (2000)
PI	$[(SiO_2/(SiO_2 + TiO_2 + Fe_2O_3 + Al_2O_3)] \times 100$	Ruxton (1968)
SF	SiO_2/Fe_2O_3	Jenny (1941)
SA	SiO_2/Al_2O_3	Ruxton (1968)
SOC	$Al_2O_3 + Fe_2O_3$	Irfan (1996)
ALK	$[K_2O/(K_2O + Na_2O)] \times 100$	Harnois and Moore (1988)
LC	$SiO_2/(K_2O + Na_2O + CaO + MgO)$	Ng et al. (2001)
CIA	$[Al_2O_3/(Al_2O_3 + CaO + Na_2O + K_2O)] \times 100$	Nesbitt and Young (1982)
Si-Ni	$[SiO_2/Al_2O_3)/((SiO_2/TiO_2) + (SiO_2/Al_2O_3) + (Al_2O_3 + TiO_2)]$	
Kr	$SiO_2/(Al_2O_3 + Fe_2O_3)$	Moignien (1966)
AKN	$Al_2O_3/(K_2O + Na_2O)$	Harnois and Moore (1988)
ACN	$Al_2O_3/(Al_2O_3 + K_2O + Na_2O)$	Harnois and Moore (1988)
MWPI	$((K_2O + Na_2O + CaO + MgO)/(SiO_2 + Al_2O_3 + Fe_2O_3 + K_2O + Na_2O + CaO + MgO)) \times 100$	Vogel (1975)
IR	CIA/WIP	Garzanti et al., 2014
R	SiO_2/Al_2O_3	Ruxton (1968)
VR	$(Al_2O_3 + K_2O)/(MgO + CaO + Na_2O)$	Vogt (1927)
CIW	$[Al_2O_3/(Al_2O_3 + CaO + Na_2O] \times 100$	Harnois (1988)
PIA	$[Al_2O_3\text{-}K_2O)/(Al_2O_3 + CaO + Na_2O\text{-}K_2O] \times 100$	Fedo et al. (1995)
STI	$[(SiO_2/TiO_2)/((SiO_2/TiO_2) + (SiO_2/Al_2O_3) + (Al_2O_3/TiO_2))] \times 100$	Jayawardena and Izawa (1994)
LOI		Suoeka et al. (1985)
	$(Na + K)/Ti$	Egli et al. (2019)
	Fe/Ti	Maher and Taylor, 1988
	$(Fe + Al)/Zr$	–
	Al_2O_3/Fe_2O_3	Jenny (1941)
	Al_2O_3/SiO_2	Xie et al. (2012)

Table 5
Average chemical composition (and standard deviation) of the investigated samples together with Δ4Si and $R^{3+}/(R^{3+} + R^{2+} + M^{+})$.

Component	Topsoil		Subsoil		River sediments	
	Average	SD	Average	SD	Average	SD
	(w.-%)	(w.-%)	(w.-%)	(w.-%)	(w.-%)	(w.-%)
Na_2O	1.81	0.29	1.74	0.30	2.28	0.27
MgO	3.13	0.53	3.11	0.73	2.65	0.18
Al_2O_3	12.90	1.29	13.17	1.83	12.12	0.70
SiO2	53.61	4.83	53.02	5.78	54.16	2.68
P_2O_5	0.27	0.16	0.19	0.08	0.24	0.04
K_2O	2.57	0.42	2.49	0.58	2.62	0.21
CaO	1.50	0.88	1.66	0.94	1.00	0.23
$CaCO_3$	7.42	3.87	9.51	8.09	8.38	3.35
TiO_2	0.70	0.08	0.70	0.09	0.70	0.04
MnO	0.16	0.04	0.17	0.07	0.16	0.05
Fe_2O_3	5.90	0.80	5.98	0.82	5.38	0.42
ZrO_2	0.02	0.00	0.02	0.00	0.02	0.00
LOI	7.10	3.03	5.91	1.79	3.97	0.49
Δ4Si	0.542	0.040	0.535	0.043	0.573	0.020
$R^{3+}/(R^{3+} + R^{2+} + M^{+})$	0.633	0.037	0.633	0.045	0.645	0.014

composition with an average SiO_2 content of about 54 weight-% (Table 5; LOI included). The variability among the different types of samples (topsoil, subsoil, river sediments) is relatively small. The samples are characterised by a relatively high Al_2O_3 and Fe_2O_3 content and some $CaCO_3$. A relatively high organic matter content (LOI) was detected not only in the soil samples but also in the river sediments. Although the geology seems to be relatively diverse in the Kan catchment, it is apparent that the chemical composition among all samples varies little (Table 5), and the differences in chemical composition between the different geological substrates are not significant. Minor differences, but significant, could be found for P_2O_5 and LOI. Substrate A seems to differ slightly from the others by showing higher contents (Fig. 3).

All samples showed similar levels of trace-element enrichment reflected in their spidergrams (Fig. 3) and are up to 200 times more enriched (Fig. 3c) than in the primitive mantle (Sun and McDonough, 1989). This enrichment is particularly pronounced for Rb, Th, U and Pr. The samples are characterised by low levels of Nb and Ti (Fig. 3), but the ratios are still >1. All samples show the same pattern, with similar ranges, indicating a similar provenance of the material. The topsoil samples, however, have in general a significantly lower Sm ratio than the subsoil and river sediments.

The DRIFT analysis enabled the detection of a wide range of minerals: also, these results confirmed the intermediate composition (with mafic to felsic components) of the soils and river sediments. Besides mafic minerals such as chlorite, felsic minerals (e.g. quartz) also were detected (quartz doublet at 780 and 800 cm^{-1} in the IR spectra). In most soils, Kaolinite or halloysite (peaks at 3620 cm^{-1} and 3694 cm^{-1} in the IR spectra), gibbsite (at 3525 cm^{-1}), chlorite (at 3581 cm^{-1}), maybe serpentinite (at 3682 cm^{-1}) together with weathering products such as sepiolite, palygorskite (at 3280 cm^{-1}) and calcite could be detected (Fig. 4).

The analysis of the weathering pattern using the M^{+}-4Si-R^{2+} ternary plot (Fig. 5) indicates a trend towards 4Si (Meunier et al., 2013). This process is accompanied by a relative enrichment of Si, a leaching of M^{+} and partially of R^{2+}. This finally will lead to a conversion to the 4Si pole, namely kaolinite that is the ultimate silicate weathering product. Kaolinite is the unique stable phyllosilicate species in extreme hydrolytic weathering environments and is the dominant secondary mineral phase in highly-weathered soils (Dixon and Weed, 1989; Meunier et al., 2013).

The reaction progression towards the kaolinite pole (Fig. 6) is measured by the difference between the compositions of unweathered and weathered samples along the chemical trend corresponding to the rock source. The Δ4Si value can be calculated either by comparing it to unweathered rock of the investigation area, or in absence of such data to the UCC (Eq. (2); Fig. 6). The measured trend is typical for (ultra)mafic rocks. The maximum stage of alteration would be reached when the parent rock is transformed into kaolinite (Δ4Si % = 100%). This would be typically the case for laterites that are predominantly composed of kaolinite and oxyhydroxides. In our case the differences between top- and subsoils seem small — with a slight tendency towards a lower weathering degree in the subsoils (Table 5). The river sediments reflect the overall composition of the soils.

4.2. PCA analysis

The PCA results obtained from the clr-transformed data are presented in Table 6 and Fig. 7. The first principal component (PC1) is positively correlated with seven of the clr-transformed components (SiO_2, TiO_2, Al_2O_3, Fe_2O_3, Na_2O, K_2O and MgO), but exhibits a strong negative correlation with CaO. The second principal component (PC2) has a positive correlation only with Fe_2O_3, MgO, Al_2O_3, and TiO_2, and a negative correlation with K_2O and CaO, SiO_2, and Na_2O. PC1 and PC2 captured 33.67% and 29.14% of the total variability, respectively. Collectively, 62.81% of the total variability is explained by these two components. There is a slightly positive relationship between most river sediments samples with PC1 and a negative correlation with PC2. The surface and subsurface samples overlap and cover a wide field in the PC1-PC2 matrix.

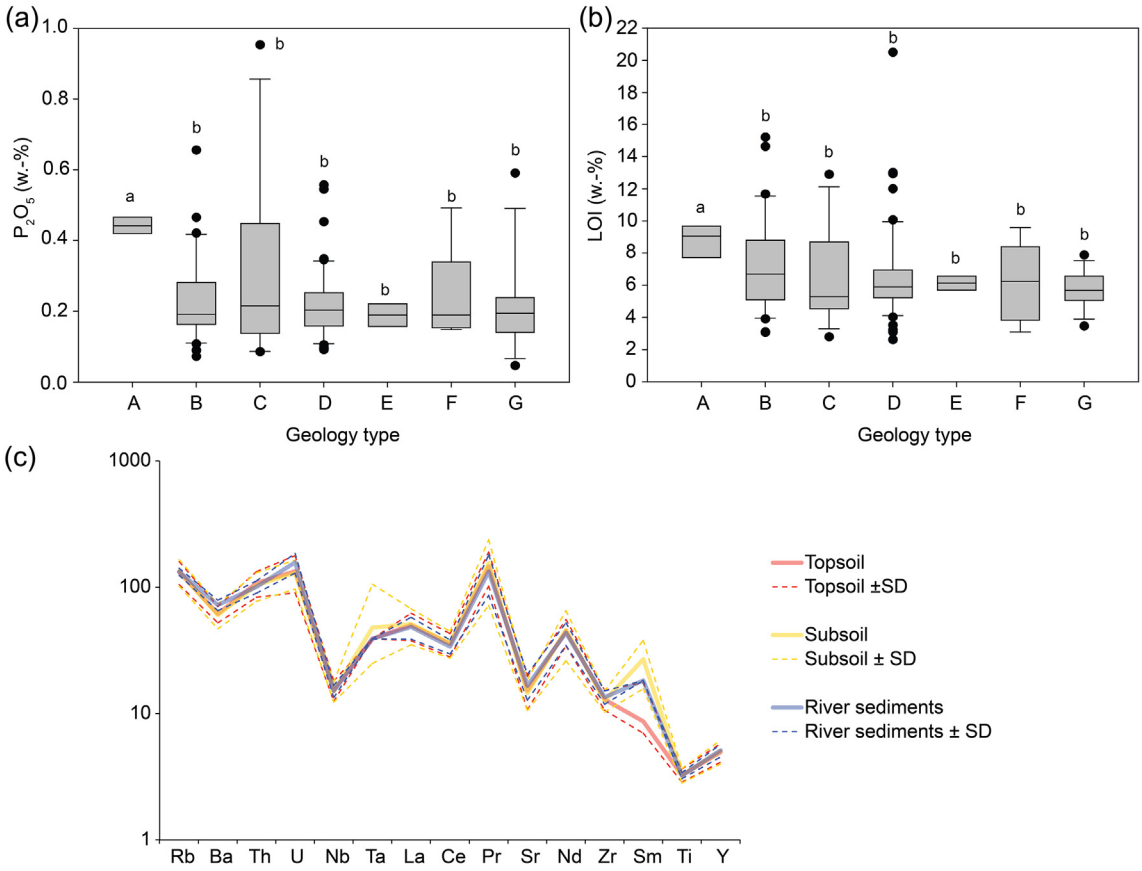

Fig. 3. Box plots for a) P_2O_5 and b) LOI as a function of the different geology types (see Table 2). The different letters indicate significant differences among the geology types tested with multiple comparison tests (nonparametric ANOVA, Kruskal-Wallis) with a significance level at $P < 0.05$. c) Incompatible trace element enrichment of topsoils, subsoil and river sediment samples in comparison to composition of the primitive mantle (Sun and McDonough, 1989).

4.3. Chemical weathering, landscape and geomorphic features

In the ternary plots (Figs. 5 and 8), the soil samples were grouped according to the main geomorphic units, geology classes, landforms and sample characteristics (river sediments, topsoil and subsoils). The geomorphic units (Fig. 8a) considerably overlap and indicate, with one exception, the presence of low to moderate weathering conditions. About 50% of the samples of the dominant geomorphic unit G2 (soils and sediments derived from solid bedrock) are nearer to the M-factor and the rest are more centrally located vector (Fig. 8a). The geomorphic unit G1 (soils and sediments derived from Quaternary deposits) has a higher proportion towards W_{min}, indicating a higher weathering degree. Fig. 8b shows that most of the samples originate from geology types B (green tuff, tuff breccia, shale tuffite with intercalations of tuffaceous siltstone), C (old and young terraces, alluvium) and A (rhyolitic tuff, lava flow, microdiorite-microgabbro as sill and dikes) distributed towards the side of the M-F vertex.

With respect to the landform type (Fig. 8c), many of the samples being attributed to type L1 are related to the corresponding geomorphic unit (G1). Samples from landform type L2 are mostly found closer to the

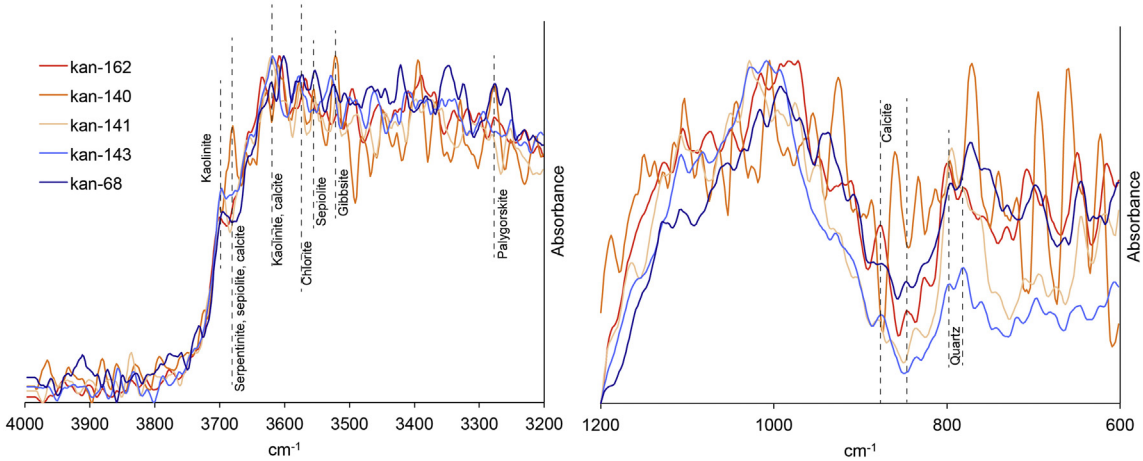

Fig. 4. DRIFT spectra for typical samples of the Kan catchment with indication of mineral bands (that potential may occur).

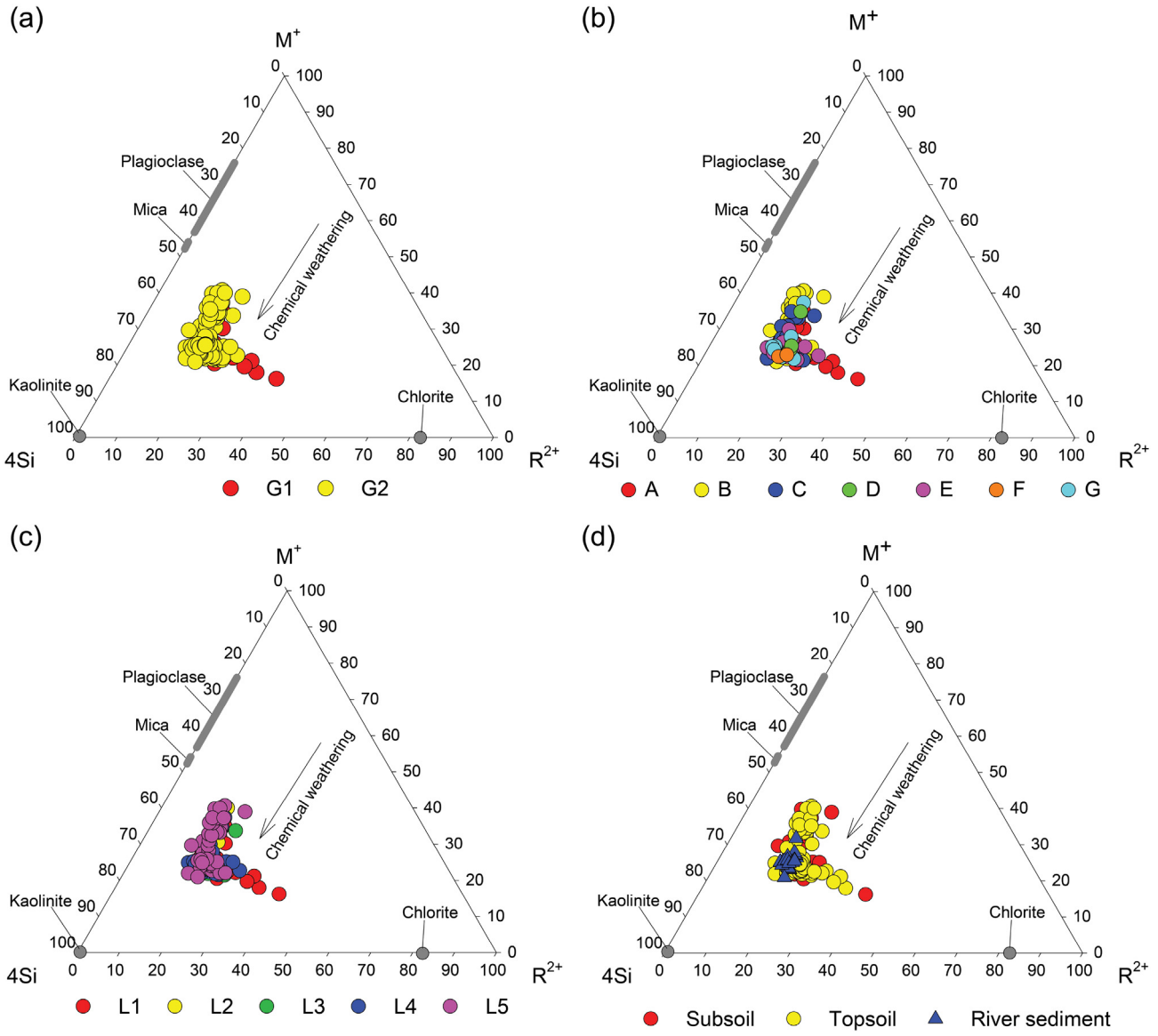

Fig. 5. Geochemical weathering plots using the 4Si-R^{2+}-M^{+} ternary diagram (according to Meunier et al., 2013 and Fang et al., 2019) for a) the major geomorphic units (G1 = 1 Quaternary deposits; G2 = solid bedrock), b) geology types (see Table 2), c) the dominant landforms (see Table 1 for details), d) the provenience of the material (subsoil, topsoil and river sediment). All plots show relative weathering intensities with black arrows denoting the trends for chemical weathering.

M-F vertex. All other landform types overlap in the ternary diagram; L4 and L5 have the highest proportion of samples and are closer to W_{min}. Fig. 8d shows that most of the river sediment samples tend to plot closer to the W_{min} vertex, indicating a higher weathering degree (Ohta and Arai, 2007; Szilas and Garde, 2013; Le Blond et al. 2015). Many of the topsoil samples are at the same position, but many also exhibit a much lower weathering degree. In general, the subsoil samples plot less often near the W_{min} vertex.

The soil and sediment samples were furthermore grouped based only on their SiO_2 content (LOI omitted and rest re-closed to 100%). This allowed a classification of the samples (Fig. 9a) into intermediate (52–63% SiO_2), intermediate-felsic (63–69% SiO_2) and felsic (> 69% SiO_2). According to the main geochemistry, soils and river sediments have predominantly intermediate to intermediate-felsic characteristics. Only a few samples are felsic. Again, no specific cluster (Fig. 9a) can be seen. The variability in terms of weathering is again very high. When plotting these data in a binary graph (Fig. 9b), then a trend of increasing weathering stages with decreasing felsic properties can be measured (according to the principal component analysis; as previously mentioned): a lower felsic proportion indicates more intense weathering.

In the 4Si-M^{+}-R^{2+} graphs, some clusters can be observed. The main geomorphic units G1 and G2 slightly differ with G1 being more in direction to the R^{2+} vertex (Fig. 5a). According to the geology, type A is slightly different from the others, extending to the R^{2+} vertex (Fig. 5b). Furthermore, the samples can be grouped based on the dominant landform type: L5 and L1 are different, with L1 tending more to R^{2+} (Fig. 5c). In general, chemical weathering in the Kan catchment proceeds in the direction to kaolinite and oxyhydroxides, and on average, the river sediments again seem to be the most weathered (Fig. 5d).

4.4. Denudation

Due to the low quartz content of the rivers sediments, we were forced to use meteoric ^{10}Be to determine denudation rates. The corresponding ^{10}Be-contents are shown in Table 7. However, the calculated denudation rates may be prone to systematic uncertainties because

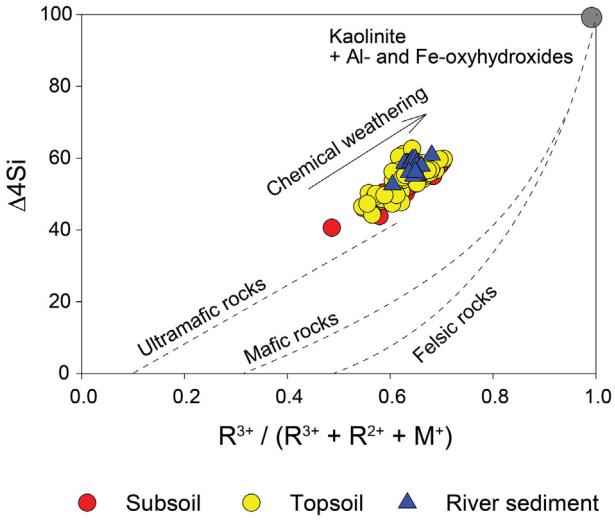

Fig. 6. Weathering reaction trend towards kaolinite, based on the difference to the maximum alteration to kaolinite (Δ4Si) and ratio to trivalent cations for the topsoil, subsoil and river sediment samples (according to Meunier et al., 2013 and Fang et al., 2019).

the input value (local ^{10}Be deposition rate) is difficult to estimate. We therefore used three different versions to estimate the input value (Table 3). The first version uses a value for that region that is roughly double that of the other two versions, which are nearly identical. The denudation rates calculated for the different sub-catchments vary by a factor of about 10. The Keshar sub-catchment has the highest denudation rates whereas lower rates were measured for both the Taloon and Davood sub-catchments. Using the modelled regional depositional flux of the first version (Field et al., 2006; Heikkilä, 2007), then the obtained erosion rates are high compared to other published values (e.g. Schaller et al., 2016), but not impossible (Heimsath et al., 2012).

The relationship between denudation rate (as a function of the different depositional fluxes) and 8 important topographic features in each sub-basin was investigated using a correlation analysis (Table 8). There is no clear correlation of erosion rates with these topographic features (p is always >0.05). There is, however, a weak relation to curvature and elevation.

4.5. Comparison of commonly used weathering indices

Based on the spatial variability of soil elements, a genetic algorithm was used to determine the best weathering indices in the four topographic clusters. The (Na + K)/Ti ratio, the WIP, the (Fe + Al)/Zr ratio and the PI seem to produce the best results. In the next step, we wanted to know if these weathering indices differ among the 4 topographic clusters using a one-way ANOVA. We found no significant differences (Table 9). The results of correlations between the various weathering indices ((Na + K)/Ti ratio, the WIP, the (Fe + Al)/Zr ratio and the PI) and a number of soil elements are given in Fig. 10. High correlations with Ca, K, Na and Al are evidently clear, because these elements are often part of the weathering index. Some indexes, however, do not use base cations such as the PI or the (Fe + Al)/Zr ratio. Interestingly, the PI index shows only a weak to a moderate correlation to Na, Mg and K. Also the (Fe + Al)/Zr ratio is only correlated to Na and Ca. In general, Al, K, Fe, Y, Zr, Nb are elements that all correlate relatively well to all indices.

Table 6
Results of the principal component analysis.

Component	PC_1	PC_2
SiO_2	0.751	−0.289
TiO_2	0.619	0.248
Al_2O_3	0.546	0.411
Fe_2O_3	0.252	0.867
MgO	0.105	0.755
CaO	−0.932	−0.290
Na_2O	0.620	−0.128
K_2O	0.347	−0.771
Eigenvalue	2.693	2.331
Variance %	33.67	29.14
Cumulative %	33.67	62.81

5. Discussion

5.1. Chemical weathering

Although the Kan catchment is characterised by several geological units, the geochemical conditions are moderately comparable. The geology type A (consisting of rhyolithic tuff and lava) has a slightly different composition (with respect to P and LOI; Fig. 3) and has a more acidic, i.e. felsic, composition.

On average, the weathering pattern of river sediments correlates in the principal component matrix slightly more to Na_2O, SiO_2 and K_2O (Fig. 7) whereas the subsoil and topsoil samples correlate more to TiO_2, Al_2O_3, CaO, Fe_2O_3 and MgO. Using the M-F-W_{min} ternary plots (Fig. 8), most of the samples indicate low-to-moderate chemical weathering conditions. The 4Si-M^+-R^{2+} diagrams (Fig. 6, Table 5) also exhibit a moderate weathering with the fluvial sediments again exhibiting an average weathering degree that is slightly higher than the top- and subsoils, although some of the topsoil samples overlap with the river sediment samples. Based on an ANOVA on ranks (Kruskal-Wallis) analysis, the river sediments have a higher average weathering degree ($P < 0.001$) than the top- and subsoil samples. The topsoil samples have a slightly higher ΔSi4 value than the subsoil samples, but this difference is not significant. In terms of soil evolution and weathering, this pattern would correspond to relatively young soils or soils having a fast turnover rate and, thus, a low residence time for soil particles. Under steady-state conditions, it is possible to define the mean residence time or turnover time of a set of particles or elements as the mass of particles or elements in the system divided by the rate of throughput (Brantley et al., 2011). The residence time of minerals within soils is sensitive to physical denudation rates in geomorphically dynamic landscapes (Almond et al., 2007; Yoo and Mudd, 2008; Šamonil et al., 2020).

The results from the fluvial sediments always overlap with those from the most-weathered topsoil samples. This indicates (see below) that the eroded material (that was transported into the fluvial sediments) predominantly derives from the topsoils. In the $R^{3+}/(R^{3+} + R^{2+} + M^+)$ vs Δ4Si diagram, the ratios from the topsoil, subsoil and river sediment samples lie more along the ultramafic rock trend and are partially close to the theoretically "forbidden" zone for weathered rock series. This effect points to multi-source sediments and soils (mixing of fresh rock debris with clays, carbonates or Fe-Al-oxyhydroxides; Meunier et al., 2013). According to Kostrzewski et al. (1997), the hydrographic network (tributaries, upstream part, etc.), floodplains, the channel perimeter (e.g., erosional bottom of the channel), biogenic elements, and man-made products contribute to dissolved and solid particles, and thus sediments, in rivers. The effect of flood plains and man-made products is negligible (due to the low population density and absence of a floodplain). The chemical signature of the river sediments indicates that they predominantly derive from eroded soil material. This is supported by the measured high erosion rates that seem to be connected to the tectonic uplift (see Section 5.2).

Weathering, mineral transformation and erosion, accumulation and in general soil redistribution seems very active in the Kan catchment. Although soil-mixing should occur, the weathering trajectories mostly trend towards the formation of kaolinite and oxyhydroxide in soils. Such a trend is often found in Mediterranean soils (Egli et al., 2019)

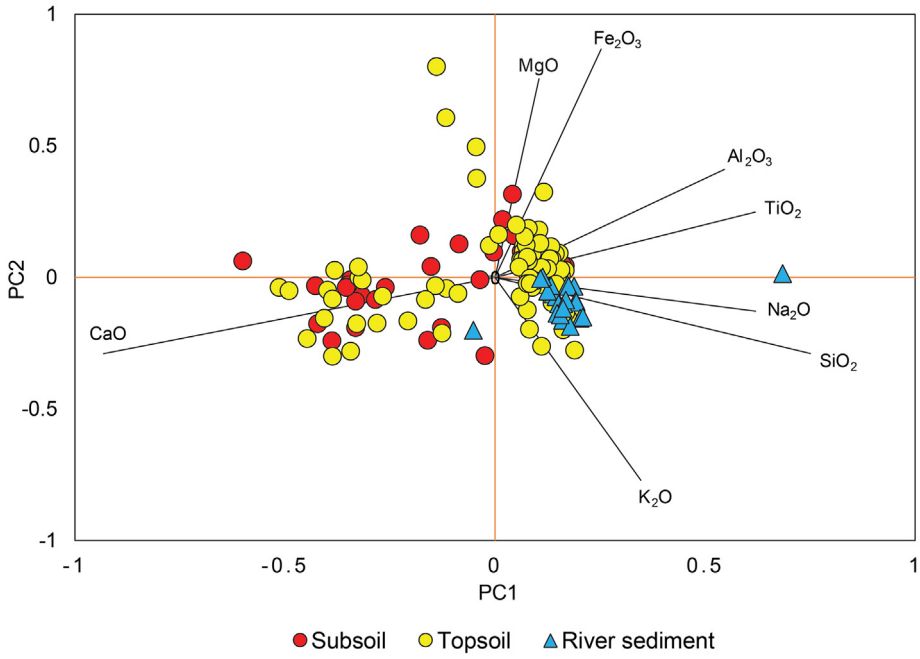

Fig. 7. Scores of samples as a function of their provenience in the PC1 and PC2 matrix together with the loading of chemical components.

and in subtropical/tropical regions (Le Blond et al., 2015). In addition, phyllosilicates such as palygorskite seem to be present that are typical weathering products in relatively dry or subarid climates (Singer, 1984; Bakhshandeh et al., 2011; Moazallahi and Farpoor, 2012).

Although the geochemical differences between the different sample types (topsoil, subsoil, river sediments) are generally small, the significantly lower Sm/Nd ratio in the topsoil samples (0.063) compared to the subsoil samples (0.193) and river sediments (0.138) probably points to some aeolian input (Viers and Wasserburg, 2004).

Finally, the relationship between weathering indices and geomorphic, geological, landform (elevation, slope and aspect) characteristics in topsoils, subsoils and river sediment was evaluated across the catchment using the M-F-W_{min} and 4Si-M^{+}-R^{2+} ternary diagrams (Meunier et al., 2013). In the Kan catchment, weathering conditions are affected by the dominant geomorphic, geological and landform characteristics. Samples from unconsolidated Quaternary deposits (G1; having the main geology types B and particularly C; Fig. 8) seem, on average, slightly more weathered than soils deriving from bedrock (G2; consisting predominantly of the Geology type D = Massive green tuff, shale with dacitic and andesitic-basaltic lava flows and landforms L5 and L4 having high elevation (2200–2800 m), steep slopes (50–100%), and eastern and western aspects). Hence, these factors determine the environmental conditions and processes of the region, and particularly the intensity of soil weathering. Chemical weathering and soil formation seem more advanced on unconsolidated sediments. Particularly at the beginning of soil evolution, soil production rates may be reduced on solid bedrock compared to sedimentary deposits (Egli et al., 2014). Astonishingly, aspect has little effect (no significant differences) on chemical weathering as represented by these weathering indices. In alpine environments, aspect usually affects weathering processes — with higher rates at the pole-facing sites — owing to differences in percolation fluxes and humidity (Egli et al., 2018; Pelletier et al., 2018).

The felsic properties of the samples are inversely related to weathering stage. In general, mafic minerals such as pyroxenes or chlorite weather faster than quartz or orthoclase: a trend that is inversely proportional to the Bowen series (Bowen, 1927). The commonly-used weathering indices did not follow these weathering trends very well. Among the tested weathering indices (Table 4), the (K + Na)/Ti ratio, the WIP, (Fe + Al)/Zr ratio and the PI indices seem to be slightly more sensitive to element variability. However, these indices did not indicate any relationship to the type of geology, geomorphic units, topographic features (e.g. slope), etc. (Table 9). Several weathering indices have genetic limitations that may complicate or impede interpretation (Meunier et al., 2013). This drawback is avoided by using the 4Si-M^{+}-R^{2+} or the M-F-W_{min} systems, which offer better discriminations of the weathering trends. By relating the $R^{3+}/(R^{3+} + R^{2+} + M^{+})$ with Δ4Si, two major weathering processes are considered: 1) the relative enrichment in silica (kaolinisation); 2) the final enrichment in insoluble components (Al_2O_3 and Fe_2O_3).

5.2. Denudation

The denudation rates displayed in Table 3 reflect catchment-wide processes (Bartley et al., 2015) and thus cannot distinguish physical soil erosion from denudation as a general degradation process, which is a combination of soil erosion, shallow landsliding, rock breakdown, weathering and mass wasting. However, the river sediments consist predominantly of weathered topsoil material (Figs. 5 and 8). This indicates that catchment-wide denudation is primarily due to physical soil erosion or shallow landsliding (Yu et al., 2019). These rates are, as previously mentioned, partially very high. Depending on the ^{10}Be depositional flux (Table 3), the erosion rates reach values of up to 0.265–0.62 mm yr^{-1}. At steep slopes of the San Gabriel Mountains (California), Heimsath et al. (2012) measured soil denudation rates up to 1 mm yr^{-1}. In regions such as the Himalaya, denudation rates are measured in the range of 0.5–2.4 mm yr^{-1} (Lupker et al., 2012). In geomorphologically or tectonically active regions, similarly high erosion or denudation rates were measured (e.g. 1.9 mm yr^{-1} in Taiwan; Siame et al., 2011). These published rates however include all erosional processes and not only soil erosion.

In terms of geology, large parts of the Kan catchment are composed of unconsolidated material, siltstone tuff, shale tuff and tuff which are relatively easily erodible. These features, along with strong elevation changes and steep slopes, affect the intensity of weathering and erosion in this region. The Kan catchment can be regarded as a remote part of the Alpine-Himalayan orogenic belt. Faults and folds of the Tehran plain have been recognised. Tehran lies at the foot of the Alborz belt, which is a seismically active region to the south of the Caspian Sea

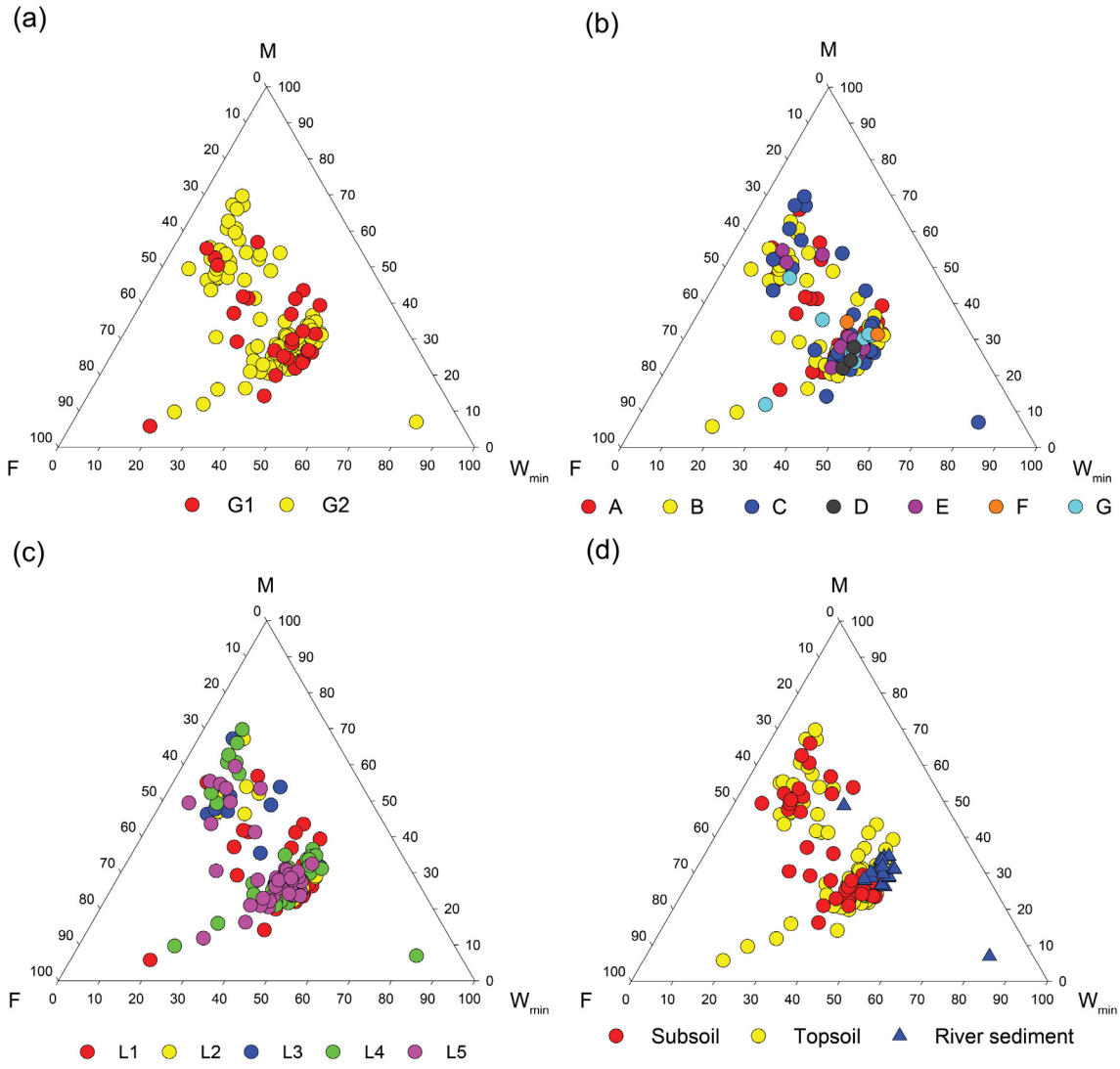

Fig. 8. Ternary diagram combining geochemical properties of the soils and river sediments (M = mafic components, F = felsic components) with W_{Min} = weathering degree (see Eqs. (5) and (6)) related to (a) the main geomorphic units (G1 = 1 Quaternary deposits; G2 = solid bedrock), (b) main geology type (see Table 2 for details), (c) dominant landform classes (see Table 1 for details) and (d) provenience of the material (subsoil, topsoil and river sediment).

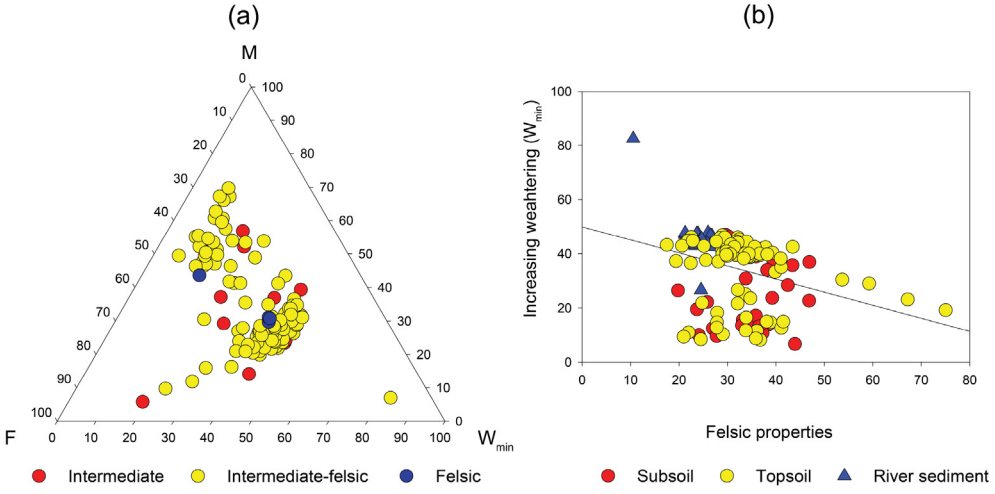

Fig. 9. a) Ternary diagram with geochemical properties and weathering degree of the soils and river sediments (M = mafic components, F = felsic components, W_{Min} = weathering degree, see Eqs. (5) and (6)) combined with a general geological characterisation of the samples (based on the SiO_2 content: intermediate = 52–63% SiO_2, intermediate felsic = 63–69% SiO_2, felsic ≥ 69% SiO_2). b) Comparison of the weathering degree with felsic properties (%) of the samples.

Table 7
^{10}Be content of the river sediments (subcatchments).

Lab sample name	^{10}Be/^{9}Be[a] (10^{-12})	SD ^{10}Be/^{9}Be[a] (10^{-12})	^{10}Be (at/g) ($\times10^{6}$)	SD ^{10}Be (at/g) ($\times10^{6}$)	SD ^{10}Be %
KAN-1	0.358	0.013	12.290	0.446	3.6%
KAN-2	0.191	0.012	6.994	0.442	6.3%
KAN-3	0.753	0.033	24.893	1.098	4.4%
KAN-4	0.345	0.015	11.182	0.498	4.5%
KAN-5	2.076	0.075	75.214	2.709	3.6%
KAN-6	2.021	0.076	68.515	2.582	3.8%
KAN-BA3 (lab blank)	0.010[b]	0.002[b]			

[a] Values corrected for laboratory blank.
[b] Values without correction for laboratory blank.

(Talebian et al., 2016). The tectonic activity in the Alborz mountain range is caused both by the northward convergence of central Iran towards Eurasia, and also by the north-westward motion of the South Caspian Basin with respect to Eurasia (Mousavi et al., 2013). Talebian et al. (2016) showed that the Tehran region has relatively rapid slip- and uplift-rates of about 1 mm yr^{-1}. As a result, steep slopes (50–100%) prevail (Fig. 2) which is typical for threshold landscapes. Such landscapes may have both continuous soil erosion and shallow landsliding (Yu et al., 2019). This explains to a great extent the high physical erosion rates of this region.

Total maximum denudation rates in the Kan catchment are in the range of 700–1670 t km^{-2} yr^{-1}. Assuming that the versions with the Q2 and Q3 ^{10}Be depositional flux (Table 3) are most likely, then the average denudation rates are in the range of 320–330 t km^{-2} yr^{-1} (with a maximum of 720–740 t km^{-2} yr^{-1}). We did not observe a close relation between erosion and topographical features, unlike, e.g. Song et al. (2019); however, a weak relation seems to exist between elevation and curvature most likely because of the small number of observations. According to the geochemistry (Figs. 5 and 8) and the chemical resemblance of river sediments and soils, denudation is mostly due to physical soil erosion. We therefore can connect denudation and soils. Soils can only form if the rate of their production is higher than the rate of denudation. Soil formation (F_{Soil}) can be expressed by.

$$F_{Soil} = P_{Soil} - D_{Soil} \quad (9)$$

where P_{Soil} = soil production and D_{Soil} = soil denudation. Progressive phases occur when soil production is greater than soil denudation, while regressive phases occur when soil denudation rates are greater than soil production. Steady state conditions are found when $F_{Soil} = 0$. In such a case we have $P_{Soil} = D_{Soil}$. Denudation (D) consists of chemical weathering fluxes (W_{Soil}) and physical erosion fluxes (E_{Soil}) with

$$D_{Soil} = W_{Soil} + E_{Soil} \quad (10)$$

Chemical and physical weathering and mineral transformation contribute to progressive soil formation, whereas strong erosion leads to regressive development and thereby to surface lowering and denudation (Raab et al., 2018). As a consequence, soil production rates are on average higher than 330 t km^{-2} yr^{-1}. It even may be — depending on the calculation procedure — that these rates are as high as 1670 t km^{-2} yr^{-1}. Such high rates are usually only found for relatively young to very young soils, where high amounts of easily weatherable minerals are present (Alewell et al., 2015). Such high values indicate that chemical weathering is at the threshold of solute transport limited to kinetically limited rates (Egli et al., 2018). High erosion rates have a similar effect and cause a constant rejuvenation of the soils: a high erosion rate usually gives rise to a high chemical weathering rate (Dixon et al., 2009; Larsen et al., 2014; Mariño et al., 2017). Chemical weathering rates are proportional to solute velocities in the soil, so solute transport mainly limits weathering and soil formation. Modelling and empirical studies (e.g. Ferrier and Kirchner, 2008; Hilley et al., 2010; Dixon and von Blanckenburg, 2012; Dixon et al., 2012) indicate that soil weathering rates are linearly coupled with denudation rates when limited by mineral supply, but kinetic limitation begins to control soil weathering as denudation rates increase and mineral residence times decrease. During early soil formation (or at very high erosion rates), chemical weathering becomes more severely limited by reaction kinetics than by solute transport. This might also be the case for the Kan catchment, although we do not have data to support this assumption.

Table 9
Results of the one-way ANOVA analysis.

Index	Topographic zone	Mean	SD	F	P
(K + Na)/Ti	Z1	13.8	1.6	1.181	0.319
	Z2	13.1	1.6		
	Z3	12.9	1.2		
	Z4	12.9	2.6		
WIP	Z1	50.8	6.0	0.704	0.551
	Z2	51.1	5.5		
	Z3	51.5	4.5		
	Z4	49.6	7.1		
(Fe + Al)/Zr	Z1	790	170.8	0.527	0.664
	Z2	794	175.1		
	Z3	762	145.9		
	Z4	747	250.2		
PI	Z1	26,781	1279.2	1.870	0.137
	Z2	27,076	1634.5		
	Z3	27,716	1783.5		
	Z4	26,787	2393.5		

WIP: Weathering index according to Parker.
PI: Product index according to Ruxton.

6. Conclusions

Based on the SiO_2 content, the soils originate mostly from an intermediate to intermediate-felsic parent material. Although the weathering trajectories all point in the direction of kaolinite and oxyhydroxides, the weathering stage of the soils and river sediments is, in general, low to moderate. The geomorphic units are connected to the landforms (in this case, lower elevations and lower slope vs higher elevations and steep slopes). The geomorphic units and landforms contribute to the spatial variability of weathering and erosion. Aspect, however, does not seem to significantly influence the weathering pattern although other investigations often demonstrate the contrary.

Many weathering indices exist, but not all of them were suitable for the investigation area. The recently developed W_{min} and Δ4Si indices appear to best discriminate the weathering trends.

Fig. 11 summarises the main processes and relationships among environmental characteristics in the Kan catchment. Although meteoric

Table 8
Correlation between erosion rates and some of topographic features (all P > 0.05).

	Profile curvature	Elevation	Flow line curvature	LS-Factor	Valley depth	Slope	TPI	Aspect
Q1	−0.352	−0.320	−0.284	−0.260	−0.245	−0.053	−0.027	0.143
Q2	−0.352	−0.318	−0.285	−0.261	−0.246	−0.054	−0.026	0.143
Q3	−0.354	−0.318	−0.283	−0.259	−0.244	−0.052	−0.029	0.144

TPI = topographical position index.
LS = slope length.
Q1–3: ^{10}Be depositional fluxes as defined in Table 3.

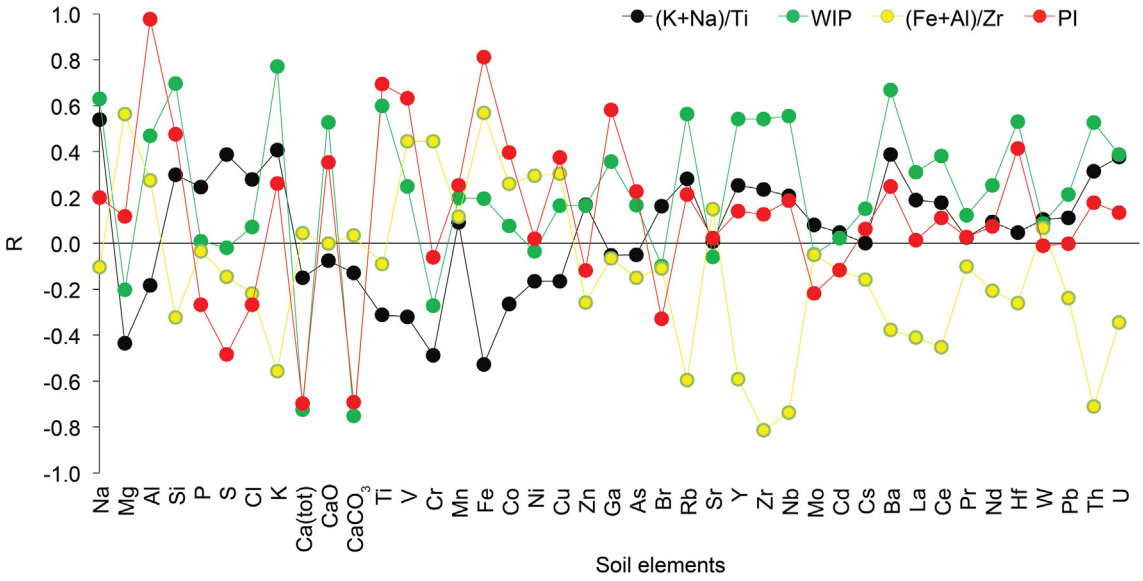

Fig. 10. Correlation scatter of the (Na + K)/Ti ratio, the WIP (weathering index according to Parker), the (Fe + Al)/Zr ratio and the PI (product index according to Ruxton) with the elements. Ca was subdivided into total Ca, Ca in silicates and carbonates.

^{10}Be holds some methodology inherent uncertainty, the denudation rates are very high in the Kan catchment, independent of the calculation procedure (depositional flux versions) used to measure them. The high erosion rates here are due mostly to high tectonic and subsequent geomorphic activities. Uplift and erosion rates are high. In addition, the strong elevation changes and steep slopes also affect the intensity of erosion, weathering and thus soil formation. At steep slopes, erosion of soil is mass wasting dominated or susceptible to shallow landsliding. Due to its dominance of steep slopes (50–100%), the Kan catchment is a threshold landscape where erosion and shallow landsliding (threshold slope angle around 30–40°; Yu et al., 2019) simultaneously occur. The soils exhibit the chemical characteristics of rather young soils, which is typical for regions with high erosion rates that lead to continuing rejuvenation of the surface and soils. Chemical weathering rates are high

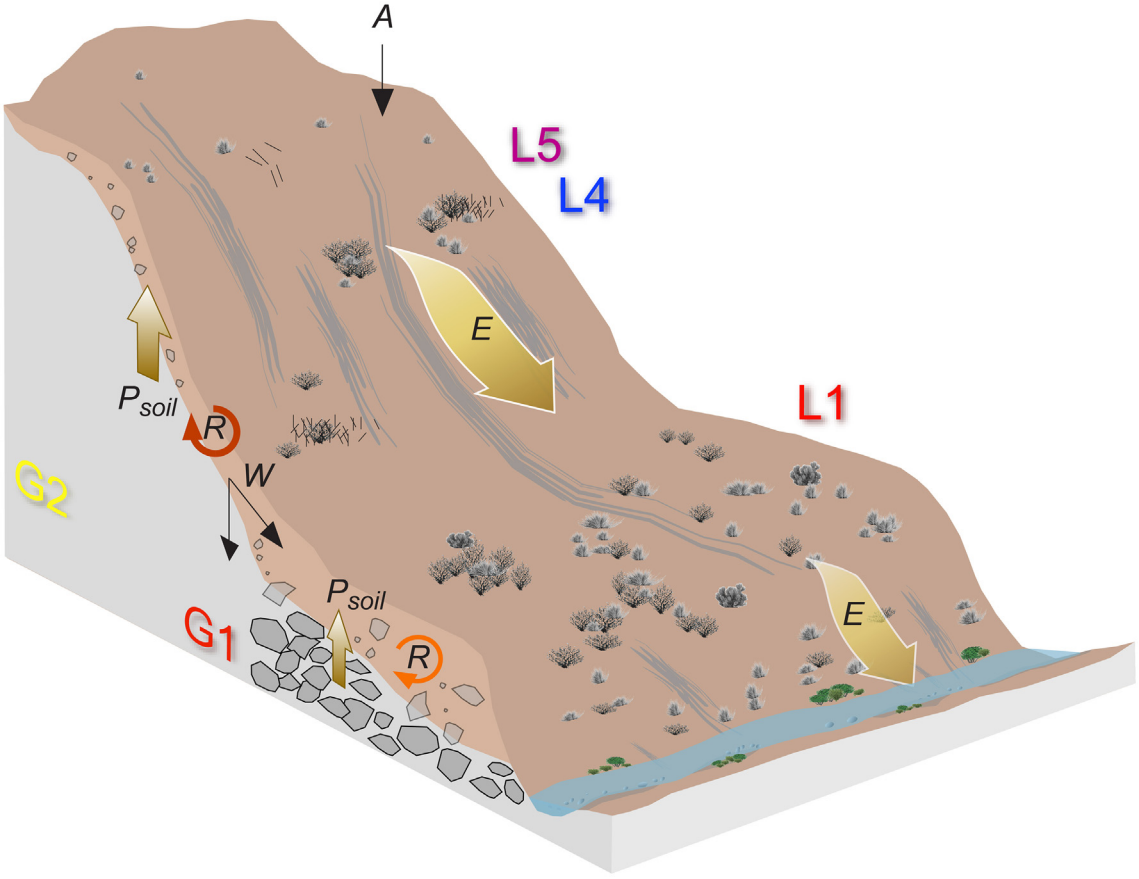

Fig. 11. Schematic process model of weathering, soil production, erosion and relation to geomorphic units (G1, G2; Table 1) and main landforms (L1, L4, L5; Table 1). W = weathering (element leaching), E = erosion, P = soil production, A = aeolian input, R = soil material turnover, residence time.

(in a steady-state, they are: 330–1670 t km^{-2} yr^{-1}) to maintain a constant soil layer. Consequently, the mean residence time of soil particles is low and the turnover rate of soil material is high.

Supplementary data to this article can be found online at https://doi.org/10.1016/j.geomorph.2020.107235.

Declaration of competing interest

The authors declare that they have no known competing financial interests or personal relationships that could have appeared to influence the work reported in this paper.

Acknowledgements

This research was supported by a grant of the "Exchange under the Cooperation with Iranian Institutions of Higher Education Scholarship, provided by Stiftung Mercator Schweiz" (University of Zurich, International Relations Office) and a "Scholarship from the Ministry of Science, Research and Technology, Islamic Republic of Iran" (Department of Scholarship and Students' Affairs Abroad, Tehran, Iran). We are furthermore grateful to Alan Rogers for the English corrections. This work was supported by the Iran Water Resources Management Company (grant number 99/005).

References

Alewell, C., Egli, M., Meusburger, K., 2015. An attempt to estimate tolerable soil erosion rates by matching soil formation with denudation in Alpine grasslands. J. Soils Sediments 15, 1383–1399. https://doi.org/10.1007/s11368-014-0920-6.

Almond, P., Roering, J., Hales, T.C., 2007. Using soil residence time to delineate spatial and temporal patterns of transient landscape response. Journal of Geophysical Research-Earth Surface 112. https://doi.org/10.1029/2006JF000568 F03S17.

Bakhshandeh, S., Khormali, F., Dordipour, E., Olamaei, M., Kehl, M., 2011. Comparing the weathering of soil and sedimentary palygorskite in the rhizosphere zone. Appl. Clay Sci. 54, 235–2541. https://doi.org/10.1016/j.clay.2011.09.007.

Bartley, R., Croke, J., Bainbridge, Z.T., Austin, J.M., Kuhnert, P.M., 2015. Combining contemporary and long-term erosion rates to target erosion hot-spots in the Great Barrier Reef, Australia. Anthropocene 10, 1–12. https://doi.org/10.1016/j.ancene.2015.08.002.

Bekaddour, T., Schlunegger, F., Vogel, H., Delunel, R., Norton, K.P., Akçar, N., Kubik, P., 2014. Paleo erosion rates and climate shifts recorded by Quaternary cut-and-fill sequences in the Pisco valley, central Peru. Earth Planet. Sci. Lett. 390, 103–115. https://doi.org/10.1016/j.epsl.2013.12.048.

Bierman, P., Steig, E.J., 1996. Estimating rates of denudation using cosmogenic isotope abundances in sediment. Earth Surf. Process. Landf. 21, 125–139. https://doi.org/10.1002/(SICI)1096-9837(199602)21:2<125::AID-ESP511>3.0.CO;2-8.

Bogunović, I., Trevisani, S., Seput, M., Juzbasic, D., Durdevic, B., 2017. Short-range and regional spatial variability of soil chemical properties in an agro-ecosystem in eastern Croatia. Catena 154, 50–62. https://doi.org/10.1016/j.catena.2017.02.018.

Bowen, N.L., 1927. The origin of ultra-basic and related rocks. American Journal of Science, Series 5 (8), 89–108.

Brantley, S.L., Megonigal, J.P., Scatena, F.N., Balogh-Brunstad, Z., Barnes, R.T., Bruns, M.A., van Cappellen, P., Dontsova, K., Hartnett, H.E., Hartshorn, A.S., Heimsath, A., Herndorn, E., Jin, L., Keller, C.K., Leake, J.R., McDowell, W.H., Meinzer, F.C., Mozdzer, T.J., Petsch, S., Pett-Ridge, J., Pregitzer, K.S., Raymond, P.A., Riebe, C.S., Shumaker, K., Sutton-Grier, A., Walter, R., Yoo, K., 2011. Twelve testable hypotheses on the geobiology of weathering. Geobiology 9, 140–165. https://doi.org/10.1111/j.1472-4669.2010.00264.x.

Breitenbach, S.F., Bernasconi, S.M., 2011. Carbon and oxygen isotope analysis of small carbonate samples (20 to 100 microg) with a GasBench II preparation device. Rapid Commun. Mass Spectrom. 25, 1910–1914. https://doi.org/10.1002/rcm.5052.

Brown, E.T., Edmond, J.M., Raisbeck, G.M., Bourlès, D.L., Yiou, F., Measures, C.I., 1992. Beryllium isotope geochemistry in tropical river basins. Geochim. Cosmochim. Acta 56, 1607–1624. https://doi.org/10.1016/0016-7037(92)90228-B.

Buggle, B., Glaser, B., Hambach, U., Gerasimenko, N., Marković, S., 2011. An evaluation of geochemical weathering indices in loess-paleosol studies. Quat. Int. 240, 12–21.

Charreau, J., Blard, P., Puchol, N., Avouac, J.-P., Lallier-Vergès, E., Bourlès, D.L., Braucher, R., Gallaud, A., Finkel, R.C., Jolivet, M., Chen, Y., Roy, P., 2011. Paleo-erosion rates in Central Asia since 9Ma: a transient increase at the onset of Quaternary glaciations? Earth Planet. Sci. Lett. 304, 85–92. https://doi.org/10.1016/j.epsl.2011.01.018.

Chmeleff, J., von Blanckenburg, F., Kossert, K., Jakob, D., 2010. Determination of the ^{10}Be half-life by multicollector ICP-MS and liquid scintillation counting. Nucl. Instrum. Methods Phys. Res., Sect. B 268, 192–199. https://doi.org/10.1016/j.nimb.2009.09.012.

Christl, M., Vockenhuber, C., Kubik, P., Wacker, L., Lachner, J., Alfimov, V., Synal, H.A., 2013. The ETH Zurich AMS facilities: performance parameters and reference materials. Nucl. Instrum. Methods Phys. Res., Sect. B 294, 29–38. https://doi.org/10.1016/j.nimb.2012.03.004.

Condie, K.C., 1993. Chemical composition and evolution of the upper continental crust: contrasting results from surface samples and shales. Chem. Geol. 104, 1–37. https://doi.org/10.1016/0009-2541(93)90140-E.

Cullers, R.L., 2000. The geochemistry of shales, siltstones and sandstones of Pennsylvanian–Permian age, Colorado, USA: implications for provenance and metamorphic studies. Lithos 51, 181–203. https://doi.org/10.1016/S0024-4937(99)00063-8.

Dixon, J.L., von Blanckenburg, F., 2012. Soils as pacemakers and limiters of global silicate weathering. Compt. Rendus Geosci. 344, 596–609. https://doi.org/10.1016/j.crte.2012.10.012.

Dixon, J.B., Weed, S.B., 1989. Minerals in Soil Environments: Madison, Wisconsin, Soil Science Society of America Book Series (1244 pp.).

Dixon, J.L., Heimsath, A.M., Amundson, R., 2009. The critical role of climate and saprolite weathering in landscape evolution. Earth Surf. Process. Landf. 34, 1507–1521. https://doi.org/10.1002/esp.1836.

Dixon, J.L., Hartshorn, A.S., Heimsath, A.M., DiBiase, R.A., Whipple, K.X., 2012. Chemical weathering response to tectonic forcing: a soils perspective from the San Gabriel Mountains, California. Earth Planet. Sci. Lett. 323–324, 40–49. https://doi.org/10.1016/j.epsl.2012.01.010.

Egli, M., Poulenard, J., 2017. Soils of mountainous landscapes. In: Richardson, D., Castree, N., Goodchild, M.M., Kobayashi, A., Liu, W., Marston, R.A. (Eds.), The International Encyclopedia of Geography. John Wiley, Sons, Ltd.. https://doi.org/10.1002/9781118786352.wbieg0197.

Egli, M., Mirabella, A., Sartori, G., Zanelli, R., Bischof, S., 2006. Effect of north and south exposure on weathering rates and clay mineral formation in Alpine soils. Catena 67, 155–174. https://doi.org/10.1016/j.catena.2006.02.010.

Egli, M., Brandová, D., Böhlert, R., Favilli, F., Kubik, P., 2010. ^{10}Be inventories in Alpine soils and their potential for dating land surfaces. Geomorphology 119, 62–73. https://doi.org/10.1016/j.geomorph.2010.02.019.

Egli, M., Norton, K., Dahms, D., 2014. Soil formation rates on silicate parent material in alpine environments: different approaches, different results? Geoderma 213, 320–333. https://doi.org/10.1016/j.geoderma.2013.08.016.

Egli, M., Hunt, A., Dahms, D., Raab, G., Derungs, C., Raimondi, S., Fang, Y., 2018. Prediction of soil formation as a function of age using the percolation theory approach. Frontiers in Environmental Science 6, 108. https://doi.org/10.3389/fenvs.2018.00108.

Egli, M., Plötze, M., Tikhomirov, D., Kraut, T., Wiesenberg, G.L.B., Lauria, G., Raimondi, S., 2019. Soil development on sediments and evaporites of the Messinian crisis. Catena 187, 104368. https://doi.org/10.1016/j.catena.2019.104368.

Fang, Q., Hong, H., Algeo, T.J., Huang, X., Sun, A., Churchman, G.J., Chorover, J., Chen, S., Liu, Y., 2019. Microtopography-mediated hydrologic environment controls elemental migration and mineral weathering in subalpine surface soils of subtropical monsoonal China. Geoderma 344, 82–98. https://doi.org/10.1016/j.geoderma.2019.03.008.

Fedo, C.M., Nesbitt, H.W., Young, G.M., 1995. Unraveling the effects of potassium metasomatism in sedimentary rocks and paleosols, with implications for paleo weathering conditions and provenance. Geology 23, 921–924. https://doi.org/10.1130/0091-7613(1995)023<0921:UTEOPM>2.3.CO;2.

Ferrier, K.L., Kirchner, J.W., 2008. Effects of physical erosion on chemical denudation rates: A numerical modeling study of soil-mantled hillslopes. Earth Planet. Sci. Lett. 272, 591–599. https://doi.org/10.1016/j.epsl.2008.05.024.

Field, C.V., Schmidt, G.A., Koch, D., Salyk, C., 2006. Modeling production and climaterelated impacts on 10Be concentration in ice cores. J. Geophys. Res. 111, D15107. https://doi.org/10.1029/2005JD006410.

Fitter, A.H., Gilligan, C.A., Hollingworth, K., Kleczkowski, A., Twyman, R.M., Pitchford, J.W., 2005. Biodiversity and ecosystem function in soil. Funct. Ecol. 19, 369–377. https://doi.org/10.1111/j.0269-8463.2005.00969.x.

Garzanti, E., Padoan, M., Setti, M., López-Galindo, A., Villa, I.M., 2014. Provenance versus weathering control on the composition of tropical river mud (southern Africa). Chem. Geol. 366, 61–74. https://doi.org/10.1016/j.chemgeo.2013.12.016.

Goovaerts, P., 1998. Geostatistical tools for characterizing the spatial variability of microbiological and physico-chemical soil properties. Biol. Fertil. Soils 27, 315–334. https://doi.org/10.1007/s003740050439.

Graly, J.A., Reusser, L.J., Bierman, P.R., 2011. Short and long-term delivery rates of meteoric 10Be to terrestrial soils. Earth Planet. Sci. Lett. 302, 329–336. https://doi.org/10.1016/j.epsl.2010.12.020.

Granger, D.E., Schaller, M., 2014. Cosmogenic nuclides and erosion at the watershed scale. Elements 10 (5), 369–373. https://doi.org/10.2113/gselements.10.5.369.

Granger, D.E., Kirchner, J.W., Finkel, R., 1996. Spatially averaged long-term erosion rates measured from in situ-produced cosmogenic nuclides in alluvial sediment. The Journal of Geology 104, 249–257. https://doi.org/10.1086/629823.

Grischott, R., 2016. Spatially and Temporally Variable Catchment-wide Denudation Rates–Clues From the Alps. Doctoral dissertation. ETH Zurich.

Grischott, R., Kober, F., Lupker, M., Hippe, K., Ivy-Ochs, S., Hajdas, I., Salcher, B., Christl, M., 2017. Constant denudation rates in a high alpine catchment for the last 6 kyrs. Earth Surf. Process. Landf. 42, 1065–1077. https://doi.org/10.1002/esp.4070.

Harnois, L., 1988. The CIW index: a new chemical index of weathering. Sediment. Geol. 55, 319–322. https://doi.org/10.1016/0037-0738(88)90137-6.

Harnois, J., Moore, J.M., 1988. Geochemistry and origin of the ore chemistry formations. A transported paleoregolith in the Grenville Province of Southern Ontario. Canada. Chem. Geol. 69, 267–289. https://doi.org/10.1016/0009-2541(88)90039-3.

Heikkilä, U., 2007. Modeling of the Atmospheric Transport of the Cosmogenic Radionuclides ^{10}Be and ^{7}Be Using the ECHAM5-HAM General Circulation Model. Ph.D. thesis. ETH-Zurich (148 pp.).

Heimsath, A.M., Dietrich, W.E., Nishiizumi, K., Finkel, R.C., 1997. The soil production function and landscape equilibrium. Nature 388, 358–361.

Heimsath, A.M., DiBiase, R.A., Whipple, K.X., 2012. Soil production limits and the transition to bedrock-dominated landscapes. Nat. Geosci. 5, 210–214. https://doi.org/10.1038/NGEO1380.

Hilley, G.E., Chamberlain, C.P., Moon, S., Porder, S., Willett, S.D., 2010. Competition between erosion and reaction kinetics in controlling silicate-weathering rates. Earth Planet. Sci. Lett. 293, 191–199. https://doi.org/10.1016/j.epsl.2010.01.008.

Horiuchi, K., Minoura, K., Kobayashi, K., Nakamura, T., Hatori, S., Matsuzaki, H., Kawai, T., 1999. Last-glacial to post-glacial ^{10}Be fluctuations in a sediment core from the Academician Ridge, Lake Baikal. Geophys. Res. Lett. 26, 1047–1050. https://doi.org/10.1029/1999GL900163.

Hunt, A.G., Ghanbarian-Alavijeh, B., Skinner, T.E., Ewing, R.P., 2015. Scaling of geochemical reaction rates via advective solute transport. Chaos 25 (075403. doi: 10.163/1.4913257).

Irfan, T.Y., 1996. Mineralogy, fabric properties and classification of weathered granites in Hong Kong. Q. J. Eng. Geol. Hydrogeol. 29, 3–35. https://doi.org/10.1144/GSL.QJEGH.1996.029.P1.02.

Jann, B., 2005. Einführung in die Statistik. 2. bearbeitete Auflage. Oldenburg Wissenschaftsverlag, München, Germany.

Jayawardena, U.S., Izawa, E., 1994. A new chemical index of weathering for metamorphic silicate rocks in tropical regions: a study from Sri Lanka. Eng. Geol. 36, 303–310. https://doi.org/10.1016/0013-7952(94)90011-6.

Jenny, H., 1941. Factors of Soil Formation: A System of Quantitative Pedology. Dover, New York (ISBN13 9780486681283).

Jungers, M.C., Bierman, P.R., Matmon, A., Nichols, K., Larsen, J., Finkel, R., 2009. Tracing hillslope sediment production and transport with in situ and meteoric 10Be. Journal of Geophysical Research Earth Surface 114 (F04020).

Korschinek, G., Bergmaier, A., Faestermann, T., Gerstmann, U., Knie, K., Rugel, G., Wallner, A., Dillmann, I., Dollinger, G., Von Gostomski, C.L., Kossert, K., Maiti, M., Poutivtsev, M., Remmert, A., 2010. A new value for the half-life of 10Be by heavy-ion elastic recoil detection and liquid scintillation counting. Nucl. Instrum. Methods Phys. Res., Sect. B 268, 187–191. https://doi.org/10.1016/j.nimb.2009.09.020.

Kostrzewski, A., Mazurek, M., Zwoliński, Z., 1997. Sources of material supply and nature of fluvial transport in post-glacial agricultural-forested catchment (the upper Parsęta river, Poland). Landform Analysis 1, 19–31.

Larsen, J.L., Almond, P.C., Eger, A., Stone, J.O., Montgomery, D.R., Malcolm, B., 2014. Rapid soil production and weathering in the Southern Alps, New Zealand. Science 343, 637–640. https://doi.org/10.1126/science.1244908.

Le Blond, J.S., Cuadras, J., Molla, Y.B., Berhanu, T., Umer, M., Baxter, P.J., Davey, G., 2015. Weathering of the Ethiopian volcanic province: a new weathering index to characterize and compare soils. Am. Mineral. 100, 2518–2532. https://doi.org/10.2138/am-2015-5168CCBY.

Liu, Y., Lee, F.H., Quek, S.T., Chen, E.J., Yi, J.T., 2015. Effect of spatial variation of strength and modulus on the lateral compression response of cement-admixed clay slab. Géotechnique 65, 851–865. https://doi.org/10.1680/jgeot.14.P.254.

Lupker, M., Blard, P.-H., Lavé, J., France-Lanord, C., Leanni, L., Puchol, N., Charreau, J., Bourlès, D., 2012. ^{10}Be-derived Himalayan denudation rates and sediment budgets in the Ganga basin. Earth Planet. Sci. Lett. 333–334, 146–156. https://doi.org/10.1016/j.epsl.2012.04.020.

Maher, B.A., Taylor, R.M., 1988. Formation of ultrafine-grained magnetite in soils. Nature 336, 368–370. https://doi.org/10.1038/336368a0.

Mariño, Y.A., Opfergelt, S., Schoonejans, J., Vanacker, V., Sonnet, P., de Jong, J., Delmelle, P., 2017. Impact of low denudation rates on soil chemical weathering intensity: A multiproxy approach. Chem. Geol. 456, 72–84. https://doi.org/10.1016/j.chemgeo.2017.03.007.

Mariotti, A., Blard, P.-H., Charreau, J., Petit, C., Molliex, S., Team, A.S.T.E.R., 2019. Denudation systematics inferred from in situ cosmogenic 10Be concentrations in fine (50–100 μm) and medium (100–250 μm) sediments of the Var River basin, southern French Alps. Earth Surface Dynamics 7, 1059–1074. https://doi.org/10.5194/esurf-7-1059-2019.

Marshall, J.A., Roering, J.J., Gavin, D.G., Granger, D.E., 2017. Late Quaternary climatic controls on erosion rates and geomorphic processes in western Oregon, USA. Geol. Soc. Am. Bull. 129, 715–731. https://doi.org/10.1130/B31509.1.

Matisoff, G., Whiting, P.J., 2011. Measuring soil erosion rates using natural (Be-7, Pb-210) and anthropogenic (Cs-137, Pu-239, Pu-240) radionuclides. In: Baskaran, M. (Ed.), Handbook of Environmental Isotope Geochemistry. 1. Advances in Isotope Geochemistry, Springer-Verlag Berlin Heidelberg, pp. 487–519. https://doi.org/10.1007/978-3-642-10637-8_25.

Meunier, A., Caner, L., Hubert, F., El Albani, A., Prêt, D., 2013. The weathering intensity scale (WIS): an alternative approach of the chemical index of alteration (CIA). Am. J. Sci. 313, 113–143. https://doi.org/10.2475/02.2013.03.

Moazallahi, M., Farpoor, M.H., 2012. Soil genesis and clay mineralogy along the xeric-aridic climotoposequence in South Central Iran. J. Agric. Sci. Technol. 14, 683–696. http://journals.modares.ac.ir/article-23-2697-en.html.

Moignien, R., 1966. Review of Research on Laterites. Natural Resources Research W. United Nations Educational, Scientific and Cultural Organization, Paris.

Morris, J., Valentine, R., Harrison, T., 2002. ^{10}Be imaging of sediment accretion and subduction along the northeast Japan and Costa Rica convergent margins. Geology 30, 59–62.

Mousavi, Z., Walpersdorf, A., Walker, R.T., Tavakoli, F., Pathier, E., Nankali, H.R.E.A., Nilfouroushan, F., Djamour, Y., 2013. Global Positioning System constraints on the active tectonics of NE Iran and the South Caspian region. Earth Planetary Science Letters 377, 287–298. https://doi.org/10.1016/j.epsl.2013.07.007.

Neall, V.E., 1977. Genesis and weathering of andosols in Taranaki, New Zealand. Soil Sci. 123 (6), 400–408.

Nesbitt, H.W., Young, G.M., 1982. Early Proterozoic climates and plate motions inferred from major element chemistry of lutites. Nature 299, 715. https://doi.org/10.1038/299715a0.

Ng, C.W.W., Guan, P., Shang, Y.J., 2001. Weathering mechanisms and indices of the igneous rocks of Hong Kong. Q. J. Eng. Geol. Hydrogeol. 34, 133–151. https://doi.org/10.1144/qjegh.34.2.133.

Nishiizumi, K., Imamura, M., Caffee, M.W., Southon, J.R., Finkel, R.C., McAninch, J., 2007. Absolute calibration of ^{10}Be AMS standards. Nucl. Instrum. Methods Phys. Res., Sect. B 25, 403–413. https://doi.org/10.1016/j.nimb.2007.01.297.

Norton, K.P., von Blanckenburg, F., Kubik, P.W., 2010. Cosmogenic nuclide-derived rates of diffusive and episodic erosion in the glacially sculpted upper Rhone Valley, Swiss Alps. Earth Surf. Process. Landf. 35, 651–662. https://doi.org/10.1002/esp.1961.

Nosrati, K., Collins, A.L., Madankan, M., 2018. Fingerprinting sub-basin spatial sediment sources using different multivariate statistical techniques and the Modified MixSIR model. Catena 164, 32–43. https://doi.org/10.1016/j.catena.2018.01.003.

Ohta, T., Arai, H., 2007. Statistical empirical index of chemical weathering in igneous rocks: a new tool for evaluating the degree of weathering. Chem. Geol. 240, 280–297. https://doi.org/10.1016/j.chemgeo.2007.02.017.

Padilla, S., López-Gutiérrez, J.M., Sampath, D.M.R., Boski, T., Nieto, J.M., García-León, M., 2018. Determination of denudation rates by the measurement of meteoric ^{10}Be in Guadiana river sediment samples (Spain) by low-energy AMS. J. Environ. Radioact. 189, 227–235. https://doi.org/10.1016/j.jenvrad.2018.04.016.

Parker, A., 1970. An index of weathering for silicate rocks. Geol. Mag. 107, 501–504. https://doi.org/10.1017/S0016756800058581.

Pavich, M.J., Brown, L., Klein, J., Middleton, R., 1984. ^{10}Be accumulation in a soil chronosequence. Earth Planet. Sci. Lett. 68, 198–204. https://doi.org/10.1016/0012-821X(84)90151-1.

Pelletier, J.D., Barron-Gafford, G.A., Guitérrez-Jurado, H., Hinckley, E.-L.S., Istanbulluoglu, E., McGuire, L.A., Niu, G.-Y., Poulos, M.J., Rasmussen, C., Richardson, P., Swetnam, T. L., Tucker, G.E., 2018. Which way do you lean? Using slope aspect variations to understand Critical Zone processes and feedbacks. Earth Surf. Process. Landf. 43, 1133–1154. https://doi.org/10.1002/esp.4306.

Portenga, E.W., Bierman, P., 2011. Understanding Earth's eroding surface with ^{10}Be. GSA Today 21, 4–10. https://doi.org/10.1130/G111A.1.

Price, J.R., Velbel, M.A., 2003. Chemical weathering indices applied to weathering profiles developed on heterogeneous felsic metamorphic parent rocks. Chem. Geol. 202, 397–416. https://doi.org/10.1016/j.chemgeo.2002.11.001.

Puchol, N., Charreau, J., Blard, P.-H., Lavé, J., Dominguez, S., Pik, R., Saint-Carlier, D., Team, A.S.T.E.R., 2017. Limited impact of Quaternary glaciations on denudation rates in Central Asia. Geol. Soc. Am. Bull. 129, 479–499. https://doi.org/10.1130/B31475.1.

Raab, G., Scarciglia, F., Norton, K., Dahms, D., de Castro Portes, R., Christl, M., Ketterer, M., Ruppli, A., Egli, M., 2018. Denudation variability of the Sila massif upland (Italy) from decades to millennia using ^{10}Be and $^{239+240}$Pu. Land Degrad. Dev. 29, 3736–3752. https://doi.org/10.1002/ldr.3120.

Raab, G., Egli, M., Norton, K., Dahms, D., Brandová, D., Christl, M., Scarciglia, F., 2019. Climate and relief-induced controls on the temporal variability of denudation rates in a granitic upland. Earth Surf. Process. Landf. 44, 2570–2586. https://doi.org/10.1002/esp.4681.

Riebe, C.S., Kirchner, J.W., Granger, D.F., Finkel, R.C., 2001. Strong tectonic and weak climatic control of long-term chemical weathering rates. Geology 29, 511–514.

Riebe, C.S., Kirchner, J.W., Finkel, R.C., 2004. Erosional and climatic effects on long-term chemical weathering rates in granitic landscapes spanning diverse climate regimes. Earth Planet. Sci. Lett. 224, 547–562.

Ruxton, B.P., 1968. Measures of the degree of chemical weathering of rocks. The Journal of Geology 76, 518–527. https://doi.org/10.1086/627357.

Šamonil, P., Egli, M., Steinert, T., Norton, K., Abiven, S., Daněk, P., Hort, L., Brandová, D., Christl, M., Tikhomirov, D., 2020. Soil denudation rates in an old-growth mountain temperate forest driven by tree uprooting dynamics, Central Europe. Land Degrad. Dev. 31, 222–239. https://doi.org/10.1002/ldr.3443.

Schaller, M., Ehlers, T.A., Stor, T., Torrent, J., Lobato, L., Christl, M., Vockenhuber, C., 2016. Spatial and temporal variations in denudation rates derived from cosmogenic nuclides in four European fluvial terrace sequences. Geomorphology 274, 180–192. https://doi.org/10.1016/j.geomorph.2016.08.018.

Sharma, A., Rajamani, V., 2000. Major element, REE, and other trace element behavior in amphibolite weathering under semiarid conditions in southern India. The Journal of Geology 108, 487–496. https://doi.org/10.1086/314409.

Siame, L.L., Angelier, J., Chen, R.-F., Godard, V., Derrieux, F., Bourlès, D.L., Braucher, R., Chang, K.-J., Chu, H.-T., Lee, J.-C., 2011. Erosion rates in an active orogen (NETaiwan): a confrontation of cosmogenic measurements with river suspended loads. Quat. Geochronol. 6, 246–260. https://doi.org/10.1016/J.QUAGEO.2010.11.003.

Singer, A., 1984. Clay formation in saprolites of igneous rocks under semi arid to arid conditions, Negev, Southern Israel. Soil Sci. 137, 332–340.

Song, C., Ji, H., Beckford, H.O., Chang, C., Wang, S., 2019. Assessment of chemical weathering and physical erosion along a hillslope, southwest China. Catena 182, 104133. https://doi.org/10.1016/j.catena.2019.104133.

Sun, S.S., McDonough, W.F., 1989. Chemical and isotopic systematics of oceanic basalts; implications for mantle composition and processes. In: Saunders, A.D., Norry, M.J. (Eds.), Magmatism in the Ocean Basins. Geological Society Special Publication. 42. Blackwell Scientific, Oxford, pp. 313–345.

Suoeka, T., Lee, I.K., Huramatsu, M., Imamura, S., 1985. Geomechanical properties and engineering classification for decomposed granite soils in Kaduna district. Nigeria. In: Proceedings of the 1st International Conference on Geomechanics in Tropical Lateritic and Saprolitic Soils. Brasilia. Brazilian Society for Soil Mechanics, Vol. 1, pp. 175–186.

Szilas, K., Garde, A.A., 2013. Mesoarchaean aluminous rocks at Storø, southern West Greenland: new age data and evidence of premetamorphic seafloor weathering of basalts. Chem. Geol. 354, 124–138. https://doi.org/10.1016/j.chemgeo.2013.07.001.

Talebian, M., Copley, A.C., Fattahi, M., Ghorashi, M., Jackson, J.A., Nazari, H., Sloan, R.A., Walker, R.T., 2016. Active faulting within a megacity: the geometry and slip rate of the Pardisan thrust in central Tehran, Iran. Geophys. J. Int. 207, 1688–1699. https://doi.org/10.1093/gji/ggw347.

Tan, X., Wang, X., Khoshnevisan, S., Hou, X., Zha, F., 2017. Seepage analysis of earth dams considering spatial variability of hydraulic parameters. Eng. Geol. 228, 260–269. https://doi.org/10.1016/j.enggeo.2017.08.018.

Viers, J., Wasserburg, G.J., 2004. Behavior of Sm and Nd in a lateritic soil profile. Geochimica et Cosmochmica Acta 68, 2043–2054. https://doi.org/10.1016/j.gca.2003.10.034.

Vogel, D.E., 1975. Precambrian weathering in acid metavolcanic rocks from the superior province. Villebon Township. South-Central Québec. Canadian Journal of Earth Sciences 12, 2080–2085. https://doi.org/10.1139/e75-183.

Vogt, T., 1927. Sulitjelmafeltets geologi og petrografi. Norges Geologiske Undersokelse 121, 1–560.

von Blanckenburg, F., 2005. The control mechanisms of erosion and weathering at basin scale from cosmogenic nuclides in river sediment. Earth Planet. Sci. Lett. 237, 462–479. https://doi.org/10.1016/j.epsl.2005.06.030.

von Blanckenburg, F., Bouchez, J., Wittmann, H., 2012. Earth surface erosion and weathering from the ^{10}Be (meteoric)/^{9}Be ratio. Earth Planet. Sci. Lett. 351, 295–305. https://doi.org/10.1016/j.epsl.2012.07.022.

Walling, D., He, Q., 1999. Improved models for estimating soil erosion rates from cesium-137 measurements. J. Environ. Qual. 28, 611–622. https://doi.org/10.2134/jeq1999.00472425002800020027x.

Wang, H.J., Shi, X.Z., Yu, D.S., Weindorf, D.C., Huang, B., Sun, W.X., Ritsema, C.J., Milne, E., 2009. Factors determining soil nutrient distribution in a small-scaled watershed in the purple soil region of Sichuan Province, China. Soil Tillage Res. 105, 300–306. https://doi.org/10.1016/j.still.2008.08.010.

Wang, B., Hicks, M.A., Vardon, P.J., 2016. Slope failure analysis using the random material point method. Géotechnique Letters 6, 113–118. https://doi.org/10.1680/jgele.16.00019.

Weiss, A.D., 2001. Topographic Position and Landforms Analysis. Conference Poster, ESRI International User Conference, San Diego, CA, USA.

Willenbring, J.K., von Blanckenburg, F., 2010. Meteoric cosmogenic beryllium-10 adsorbed to river sediment and soil: applications for Earth-surface dynamics. Earth Sci. Rev. 98, 105–122. https://doi.org/10.1016/j.earscirev.2009.10.008.

Wittmann, H., Malusà, M.G., Resentini, A., Garzanti, E., Niedermann, S., 2016. The cosmogenic record of mountain erosion transmitted across a foreland basin: source-to-sink analysis of in situ 10Be, 26Al and 21Ne in sediment of the Po river catchment. Earth Planet. Sci. Lett. 452, 258–271. https://doi.org/10.1016/j.epsl.2016.07.017.

WRI (Water Resources Institute of Iran), 2012. Comprehensive Flood Management (Case Study: Kan River Watershed).

Xiao, T., Li, D.Q., Cao, Z.J., Tang, X.S., 2017. Full probabilistic design of slopes in spatially variable soils using simplified reliability analysis method. Georisk: Assessment and Management of Risk for Engineered Systems and Geohazards 11, 146–159. https://doi.org/10.1080/17499518.2016.1250279.

Xie, J., Xiao, Z.F., Zheng, W.H., Liu, Y., Cheng, J.S., 2012. The effect of Al_2O_3/SiO_2 on the structure and properties of Na_2O-CaO-Al_2O_3-SiO_2 glasses. Key Eng. Mater. 509, 339–345. https://doi.org/10.4028/www.scientific.net/KEM.509.339.

Yoo, K., Mudd, S.M., 2008. Discrepancy between mineral residence time and soil age: implications for the interpretation of chemical weathering rates. The Geological Society of America 36, 35–38. https://doi.org/10.1130/G24285A.1.

Yu, F., Hunt, A., Egli, M., Raab, G., 2019. Comparison and contrast in soil depth evolution for steady-state and stochastic erosion processes: possible implications for landslide prediction. Geochemistry, Geophysics, Geosystems G3 20, 2886–2906. https://doi.org/10.1029/2018GC008125.